ADVANCED MATERIALS
www.advmat.de

Design of Local Atomic Environments in Single-Atom Electrocatalysts for Renewable Energy Conversions

Tao Sun, Sharon Mitchell, Jing Li, Pin Lyu, Xinbang Wu, Javier Pérez-Ramírez, and Jiong Lu**

Single-atom electrocatalysts (SAECs) have recently attracted tremendous research interest due to their often remarkable catalytic responses, unmatched by conventional catalysts. The electrocatalytic performance of SAECs is closely related to the specific metal species and their local atomic environments, including their coordination number, the determined structure of the coordination sites, and the chemical identity of nearest and second nearest neighboring atoms. The wide range of distinct chemical bonding configurations of a single-metal atom with its surrounding host atoms creates virtually limitless opportunities for the rational design and synthesis of SAECs with tunable local atomic environment for high-performance electrocatalysis. In this review, the authors first identify fundamental hurdles in electrochemical conversions and highlight the relevance of SAECs. They then critically examine the role of the local atomic structures, encompassing the first and second coordination spheres of the isolated metal atoms, on the design of high-performance SAECs. The relevance of single-atom dopants for host activation is also discussed. Insights into the correlation between local structures of SAECs and their catalytic response are analyzed and discussed. Finally, the authors summarize major challenges to be addressed in the field of SAECs and provide some perspectives in the rational construction of superior SAECs for a wide range of electrochemical conversions.

1. Introduction

Single-atom catalysts (SACs) have emerged as a new frontier in the field of heterogeneous catalysis due to their distinct and remarkable performance in many industrially relevant thermo-, photo-, and electrochemical conversions. In conventional heterogeneous catalysts based on metal nanoparticles, efficiencies per metal site are a few orders of magnitude lower than those of homogenous catalysts as only a small portion of metal atoms are exposed to the reaction medium. SACs with atomically dispersed metal atoms have attracted intensive research interest because of their potentially unique reactivity and maximized atom usage that combine the merits from both homogeneous and heterogeneous catalysts for efficient chemical transformation and energy conversion.[1–5] Due to the relevance for diverse sustainable energy technologies including fuel cells, water-splitting devices, and metal–air batteries,[5–9] single-atom electrocatalysis (SAECs) has evolved into one of the most active research fields for renewable energy conversions.[5,6,10–12] The major focus of this field currently lies in the rational design of SAECs with an abundance of robust and highly active sites to enhance the efficiency of the underlying electrochemical conversions to levels amenable for practical implementation.

Individual active sites of SACs consist of an isolated metal atom bonded to adjacent atoms in the host material. The unique local atomic environment plays a decisive role in determining the activity, selectivity, and stability in electrocatalytic conversions.[10–14] Due to strong chemical hybridization with atoms in the vicinity of the supported single atoms, the electronic properties and chemical stability are distinct from extended metallic ensembles in nanoparticles.[13,14] Concomitantly, the structural and electronic properties of the host are also modified by the anchored single atoms.[15,16] To date, two classes of hosts have been widely used to synthesize SAECs, i.e., carbon-based materials including carbon nanotubes, graphene, graphitic carbon-nitride (g-C_3N_4) and porous carbons,[13–18] and metal-containing compounds such as oxides, dichalcogenides, carbides, and nitrides.[13,14,19,20] The abundance of host materials offers vast opportunities in engineering the local environment of

Dr. T. Sun, Dr. J. Li, P. Lyu, X. B. Wu, Prof. J. Lu
Department of Chemistry
National University of Singapore
3 Science Drive 3, Singapore 117543, Singapore
E-mail: chmluj@nus.edu.sg

Dr. T. Sun, Dr. J. Li, Prof. J. Lu
Centre for Advanced 2D Materials and Graphene Research Centre
National University of Singapore
Singapore 117546, Singapore

Dr. S. Mitchell, Prof. J. Pérez-Ramírez
Institute for Chemical and Bioengineering
Department of Chemistry and Applied Biosciences
ETH Zürich
Vladimir-Prelog-Weg 1, Zürich 8093, Switzerland
E-mail: jpr@chem.ethz.ch

Prof. J. Pérez-Ramírez
Department of Chemical and Biomolecular Engineering
National University of Singapore
4 Science Drive 4, Singapore 117585, Singapore

The ORCID identification number(s) for the author(s) of this article can be found under https://doi.org/10.1002/adma.202003075.

DOI: 10.1002/adma.202003075

single-metal atoms into desired active sites for electrocatalytic reactions. Because of this, high-performance SAECs with a large variety of architectures have been reported, in some cases even outperforming commercial precious-metal-based catalysts.

Since the first report of SACs in 2011,[1] this field has progressed rapidly introducing new synthetic approaches, developing knowledge related to the design and identification of novel active sites, and exploring the reactivity in diverse applications. To date, most review articles focus on methods for the preparation and the unique catalytic properties of SACs.[4–6,10,11,13–16] The impact of the local environment on the performance of SACs has not been systematically examined. This review summarizes recent progress on understanding and engineering the active site structures of SAECs to deliver superior catalytic technologies (**Figure 1**). This is highlighted in the area of renewable energy, where single atoms have shown great promise to optimize the adsorption energies of intermediates over commonly studied transition metals in bulk form. To set the scene, we first introduce the prominent reactions including oxygen reduction, hydrogen evolution, oxygen evolution, nitrogen reduction, and carbon dioxide reduction underpinning energy conversion technologies, identifying the main challenges for catalyst design (Table 1). We then discuss local structures of both precious and nonprecious metal-based SAECs, encompassing the first (directly bonded with the single-metal atom) and second (not directly bonded with the single-metal atom) coordination spheres and beyond, as well as analyzing their electrocatalytic roles. Besides examining how the properties of single atoms can be engineered by controlling the surrounding structure of the host, we explore how single-atom doping has been adopted to tune the crystalline phase and electronic properties of host materials for enhanced electrocatalysis. Finally, we put forward some future perspectives related to the structural engineering of the desired local environment of SAECs.

2. Challenges in Electrocatalyst Design for Renewable Energy Conversions

2.1. Oxygen Reduction Reaction (ORR)

Oxygen reduction reaction occurring at the cathode of fuel cells is one of the most important reactions for energy conversion.

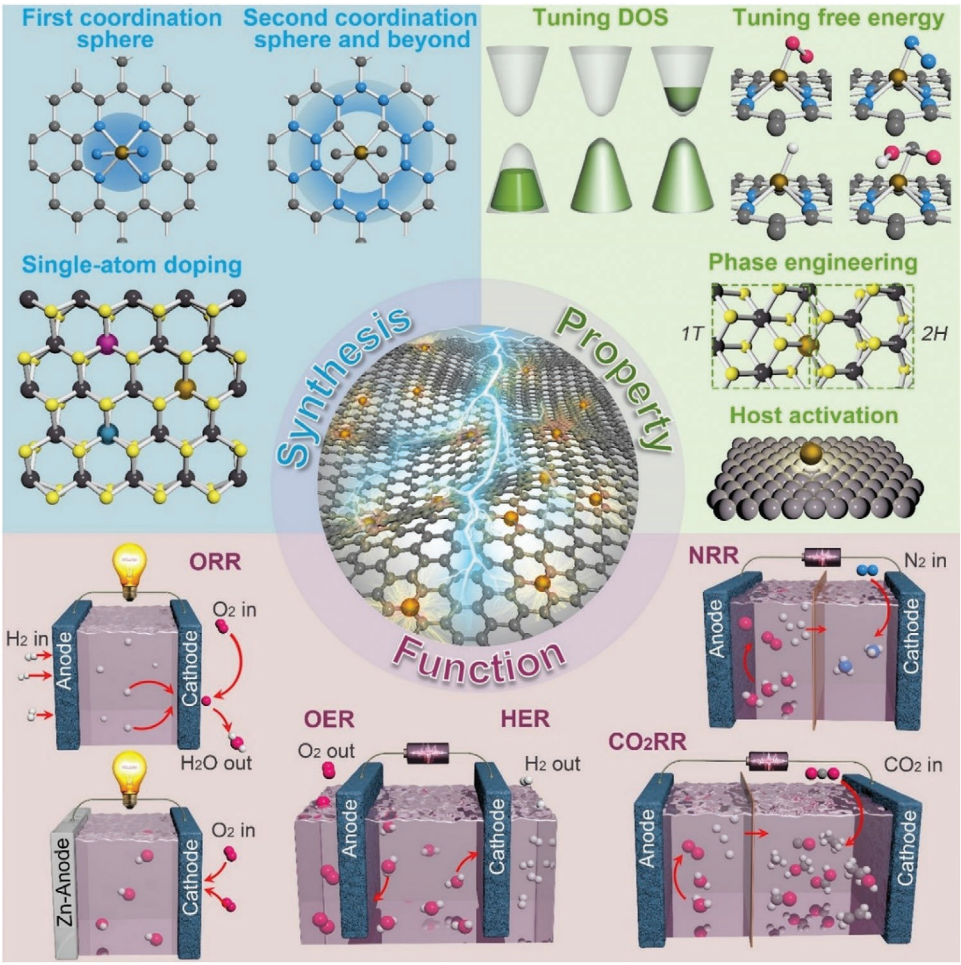

Figure 1. Engineering the local atomic environments of single-atom electrocatalysts (SAECs) for applications in renewable energy conversions, including ORR, OER, HER, NRR, and CO_2RR. Common strategies such as tailoring the first or second coordination sphere and beyond, and single-atom doping permit modification of the density of states (DOS) of isolated metal centers in SAECs, and the associated free energy profile of reactants, intermediates and final products, as well as the phase engineering and/or activation of the host.

Due to its sluggish kinetics, the ORR is considered as the potential-limiting step and thus plays a vital role in determining the overall performance of fuel cell devices.[21,22] In aqueous electrolytes, the ORR proceeds through one of two reaction pathways depending on the reaction medium used (Table 1).[22–24] Typically, it follows a 4-electron pathway for the reduction of O_2 into H_2O (acidic media) or OH^- (alkaline media) with an equilibrium potential of 1.23 V versus reversible hydrogen electrode (RHE). However, hydrogen peroxide (H_2O_2) or peroxide species (OOH^-) can be generated via a 2-electron pathway in acidic or alkaline media, respectively. The production of H_2O_2 or OOH^- not only reduces the efficiency of chemical energy conversion, but also results in corrosion of the fuel cell components including the membrane and structural framework with supporting catalysts and collector plates.[25,26] Therefore, a superior ORR electrocatalyst should not promote 2-electron pathways.

Based on thermodynamics, an ideal ORR process should have a free energy drop of –1.23 eV for each step.[27] In this case, there is no overpotential for ORR with a $4e^-$ pathway (electron transfer number $n = 4$). In practical systems, energy barriers for the formation of intermediates (OOH*, OH*, and O* species) exist in each reaction step, and they differ from each other, resulting in an overpotential (voltage loss) that reduces the potential output of a fuel cell. Recent reports show that the formation of OOH* or the desorption of OH* intermediate species are the potential-limiting steps of ORR in many practical systems.[22–24,27–29] Pt and its alloys are known to be efficient ORR catalysts due to their excellent activity and selectivity. However, the prohibitive cost, scarcity, and susceptibility to CO poisoning of Pt hamper the large-scale deployment of electrocatalysts based on this metal. According to the report of the United States Council for Automotive Research LLC, the price of Pt in a hydrogen-oxygen fuel cell reaches up to \$58 kW^{-1}, thus comprising the most expensive component in the fuel cell.[30] The development of highly efficient catalysts with low Pt loading or Pt-free materials still represents a longstanding research goal.

Fuel cells can be divided into two categories depending on the working condition, i.e., polymer electrolyte membrane fuel cell (PEMFC) and alkaline fuel cell (AFC). Compared to AFC, PEMFC has unique advantages with natural CO_2 tolerance and high volumetric power. In contrast to operation in alkaline media, the presence of protons in acidic media makes it more challenging for the conversion of adsorbed O_2 into O_2^- (prior to the formation of OOH*).[31,32] Moreover, the coadsorption of ClO_4^-, Cl^-, $HCOO^-$, and SO_4^{2-} anions on the catalyst surface further slows the reaction in acidic compared to alkaline media,[31,33] which can be attributed to the physical blocking of the active sites by these adsorbents. These two limiting factors often result in a higher overpotential when the reaction is conducted in acidic rather than alkaline media.[31–33] However, the adsorption of hydroxyl anions can optimize the free energies of intermediates during the reaction and thus improve ORR activity.[33] According to the Markovic principle,[31] the overpotential of the ORR increases as the electrolyte pH decreases. Therefore, it is more challenging but highly valuable to develop high-performance ORR catalysts under acidic conditions.

2.2. Hydrogen Evolution Reaction (HER)

Water splitting provides an efficient route for the production of a clean alternative to the steam reforming of hydrocarbons for the production of H_2. In particular, highly efficient HER electrocatalysis ($2H^+ + 2e^- \rightarrow H_2$) represents a promising approach for water splitting.[34,35] As shown in Table 1, the HER consists of three possible reaction steps including the adsorption of hydrogen (Volmer reaction) and the desorption of H* (Heyrovsky or Tafel reactions).[36,37] Two primary mechanisms, the Tafel–Volmer and the Heyrovsky–Volmer, generally dominate the HER process. The rate-determining step strongly depends on the inherent chemical and electronic properties of the catalytic active sites,[38–40] and can be determined by evaluating the Tafel slope values from the HER polarization curves.[38]

It is well known that the chemical adsorption and desorption of H* on the electrode surface are competitive processes. According to the Nørskov principle,[38] a good HER catalyst should bond to adsorbed H* with sufficient strength to facilitate the proton–electron-transfer process. On the other hand, the binding of H* with the metal should be weak enough to ensure the ready desorption of the H_2 formed. Therefore, the free energy change for the adsorption of H* over the catalyst surface (ΔG_{H*}) should be close to zero. A more negative value of ΔG_{H*} means a stronger H* adsorption, while a more positive value of ΔG_{H*} indicates weaker adsorption of H*. In either case, it becomes more difficult for HER to proceed due to the presence of a large overpotential. It is noted that the barrier of hydrogen adsorption is higher under alkaline conditions due to the lack of protons.[41–43] As the pH increases, the energy barrier toward the formation of M−H* via water dissociation (Volmer reaction) gradually increases, leading to an increase of the overpotential in HER.[43] Therefore, it remains a big challenge to develop robust and efficient electrocatalysts for the activation of H_2O to form H* species in alkaline conditions.

Exchange current density (j_0) and Tafel slope are two key parameters used to evaluate the HER performance of electrocatalysts. Generally, a "volcano" curve can be established between the experimental j_0 value and the quantum chemistry-derived ΔG_{H*} for a wide range of electrode surfaces.[35,38] Several factors influence j_0 including the electrode materials and surface state, the electrolyte composition, and the reaction temperature, which serves as a direct descriptor to assess the catalytic efficiency. A standard formula describes the relationship between j_0 and Tafel plot ($\eta = b \log j_0 + a$, where η is overpotential, j_0 is the current density, and b is the Tafel slope).

2.3. Oxygen Evolution Reaction (OER)

The oxygen evolution reaction ($2H_2O \rightarrow 4H^+ + 4e^- + O_2$) is the anodic reaction for electrochemical water splitting. In this application, is recognized as a critical bottleneck due to its much slower kinetics compared to the HER, which thus determines the overall hydrogen-production efficiency.[44,45] Besides, the OER also plays a vital role in many rechargeable batteries, such as zinc–air and lithium–air batteries.[46] The reaction involves a four-electron process because the

Table 1. Comparison of the elementary steps of ORR, HER, and OER in acidic and alkaline media (* represents an adsorbed species over the active site of the catalyst at the electrode (M)).

Reaction	Acidic media	Alkaline media
ORR	$O_2 + M + H^+ + e^- \rightarrow M{-}OOH^*$	$O_2 + M + H_2O + e^- \rightarrow M{-}OOH^* + OH^-$
	$M{-}OOH^* + H^+ + e^- \rightarrow M{-}O^* + H_2O$	$M{-}OOH^* + e^- \rightarrow M{-}O^* + OH^-$
	$M{-}O^* + H^+ + e^- \rightarrow M{-}OH^*$	$M{-}O^* + H_2O + e^- \rightarrow M{-}OH^* + OH^-$
	$M{-}OH^* + H^+ + e^- \rightarrow M + H_2O$	$M{-}OH^* + e^- \rightarrow M + OH^-$
	$O_2 + 4H^+ + 4e^- \rightarrow 2H_2O$ (overall)	$O_2 + 2H_2O + 4e^- \rightarrow 4OH^-$ (overall)
HER	$H^+ + M + e^- \rightarrow M{-}H^*$ (Volmer reaction)	$H_2O + M + e^- \rightarrow M{-}H^* + OH^-$ (Volmer reaction)
	$M{-}H^* + H^+ + e^- \rightarrow M + H_2$ (Heyrovsky reaction)	$M{-}H^* + H_2O + e^- \rightarrow M + H_2 + OH^-$ (Heyrovsky reaction)
	or $2M{-}H^* \rightarrow 2M + H_2$ (Tafel reaction)	or $2M{-}H^* \rightarrow 2M + H_2$ (Tafel reaction)
	$2H^+ + 2e^- \rightarrow H_2$ (overall)	$2H_2O + 2e^- \rightarrow H_2 + 2OH^-$ (overall)
OER	$H_2O + M \rightarrow M{-}OH^* + H^+ + e^-$	$M + OH^- \rightarrow M{-}OH^* + e^-$
	$M{-}OH^* \rightarrow M{-}O^* + H^+ + e^-$	$M{-}OH^* + OH^- \rightarrow M{-}O^* + H_2O + e^-$
	$M{-}O^* + H_2O \rightarrow M{-}OOH^* + H^+ + e^-$	$M{-}O^* + OH^- \rightarrow M{-}OOH^* + e^-$
	$M{-}OOH^* \rightarrow M + O_2 + H^+ + e^-$	$M{-}OOH^* + OH^- \rightarrow M + O_2 + H_2O + e^-$
	$2H_2O \rightarrow O_2 + 4H^+ + 4e^-$ (overall)	$4OH^- \rightarrow O_2 + 2H_2O + 4e^-$ (overall)

generation of one oxygen molecule requires the transfer of $4e^-$ and $4H^+$ from water. The typical reaction steps in acidic and alkaline media are summarized in **Table 1**.[45,47] The thermodynamic equilibrium potential of the water-splitting reaction is $E^0 = -1.23$ V. The stepwise oxidation of water toward O_2 production requires a high energy input to drive this reaction. Generally, the electrode potential for the oxidation of water involving four electrons and four protons is significantly lower than that of a one-electron step. In a neutral solution, the potential for the oxidation of water to *OH via the one-electron process is −2.32 V, more negative than that of the concerted four-electron oxidation (−0.815 V).[48] Therefore, OER (the involved four-electron reaction) generally exhibits a larger overpotential than that of HER,[45] a critical step for determining the overall efficiency of the hydrogen-production in water splitting devices.

The relationship between current density (j) and η can be described by the Butler–Volmer equation[49,50]

$$j = j_0\left[\exp\left(\alpha_a nF\eta/RT\right) - \exp\left(-\alpha_c nF\eta/RT\right)\right] \quad (1)$$

where j_0 is the exchange current density, n is the number of transferred electrons, F is the Faraday's constant, R is the universal gas constant, T is the thermodynamic temperature, α_a and α_c are the transfer coefficient of anodic and cathodic reactions, respectively. α_a and α_c can be assumed to be 0.5. The cathodic current can be negligible when the anodic overpotential is sufficiently large. This leads to a simplified equation of

$$j = j_0 \times \exp\left(\alpha_a nF\eta/RT\right) \quad (2)$$

which can be further converted to

$$\log j = \log j_0 + (\eta/b), \quad b = (2.303RT/\alpha nF) \quad (3)$$

where b is the Tafel slope associated with α, from which the transfer coefficient and the OER mechanism can be extracted. In addition, each OER step under different reaction conditions has one particular η value, ranging from $RT/(4F)$ to $2RT/F$.[50,51] The Faradaic efficiency (FE) is another parameter for evaluating the overall performance of an OER catalyst. FE is defined as the molar ratio of produced oxygen (n_{O_2}) to the theoretical value

$$\left(n_{O_2^{\cdot}}\right), \left\{\mathrm{FE} = n_{O_2}/n_{O_2^{\cdot}} = 4Fn_{O_2}/(It)\right\} \quad (4)$$

where I is the constant oxidation current, t is the active time at the constant oxidation current, and F is the Faraday constant.

As mentioned, the overpotential of the HER is lower in acidic than in alkaline medium. Hence, it is highly desired to develop OER catalysts used in acidic medium for water splitting to produce hydrogen. It has been reported that nonprecious metal catalysts including Fe-, Co-, Ni-, and Mn-based oxides and layered double hydroxides exhibit excellent OER catalytic activity, superior to the commercial catalysts (20% Ir/C or RuO_2) in alkaline medium.[52,53] Unfortunately, these nonprecious metal OER catalysts tend to dissolve in acidic medium, resulting in activity losses. Therefore, this calls for the development of highly efficient and robust OER catalysts used in acidic medium for electrochemical water splitting.

2.4. Nitrogen Reduction Reaction (NRR)

The electrochemical nitrogen reduction reaction ($N_2 + 6H^+ + 6e^- \rightarrow 2NH_3$) emerges as a promising decentralized approach for the synthesis of ammonia in contrast to the energy intensive Haber–Bosch process that requires high temperature (300–500 °C) and pressure (200–300 atm).[54–57] The NRR involves a six-electron and a six-proton transfer process with two types of proposed mechanism, i.e., dissociative or associative (**Figure 2**).[54,56] In the dissociative pathway, the dissociative adsorption of a N_2 molecule results in the formation of two adsorbed N atoms on the catalyst surface. The adsorbed N atoms undergo independent protonation before their conversion into NH_3 molecules. In the associative pathway, a N_2 molecule first binds to the catalyst surface followed by the hydrogenation to form N=N−H* species. The subsequent hydrogenation process can occur through two possible pathways (i.e., distal or alternating) after the formation of N=N−H* species. In the distal pathway, hydrogenation occurs preferentially on the N further away from the catalyst surface (assuming an end-on coordination mode of the N_2 molecule), leading to the release of one NH_3 molecule. The remaining metal nitrido (M≡N) species undergoes further protonation to generate a second NH_3 molecule. In the alternating pathway, monohydrogenation alternates between the two N centers over the catalyst surface till the formation of the first NH_3 molecule. The

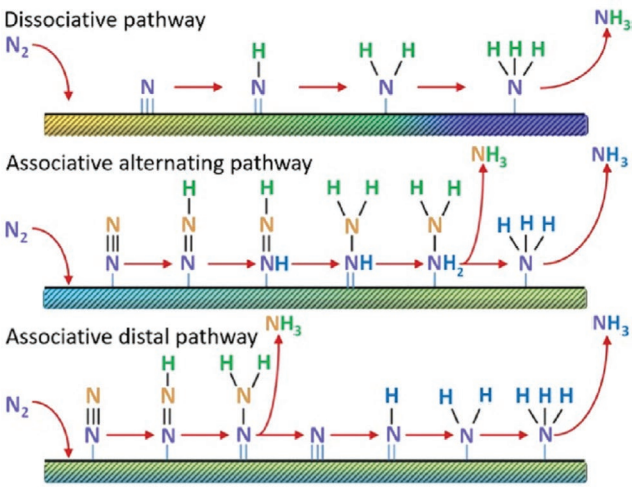

Figure 2. Proposed mechanisms of the NRR. Reproduced with permission.[56] Copyright 2017, Elsevier.

subsequent protonation of the remaining N species produces the second NH_3 molecule. A deeper understanding of the NRR mechanism via a combination of theoretical and experimental efforts will benefit the development of highly efficient catalysts with optimized performance.[58–60]

The selectivity toward NH_3 production is a key indicator of the NRR performance,[61,62] i.e., the Faradaic efficiency (FE), which is defined as the molar ratio of produced NH_3 (n_{NH3}) to the theoretical value ($n_{NH3'}$). However, the HER competes with nitrogen reduction in the same potential range, which tends to decrease the FE of NH_3 production. Therefore, a superior catalyst needs to be designed to suppress the HER and to maximize the NH_3 yield. Typically, the adsorption and activation of N_2 to form chemically adsorbed N≡N* species constitute two critical steps for the NRR.[63] In general, N_2 activation over the catalytic center is often regarded as the potential-limiting step.[64–66] For example, carbon-supported Ti–N_4 and V–N_4 catalytic centers are predicted to be highly active for N_2 activation because of a strong back-donation between the hybridized *d*-orbitals of metal center and π^* orbital of N≡N*.[67] Moreover, this work revealed that an excellent NRR catalyst should strongly adsorb N_2* and H* to activate N_2 ($\Delta G_{N2*} < 0$) and suppress H_2 generation (negative value of ΔG_{H*}), respectively.

2.5. Carbon Dioxide Reduction Reaction (CO_2RR)

The electrochemical reduction of carbon dioxide (CO_2RR) to gaseous species or energy-dense liquid fuels offers a promising strategy for both energy storage and the global carbon balance.[6,68–71] Multiple possible reaction pathways occur for the CO_2RR in aqueous electrolytes, leading to the generation of various value-added products including carbon monoxide (CO), formic acid (HCOOH) or formate ($HCOO^-$) in alkaline solution, formaldehyde (CH_2O), methanol (CH_3OH), oxalic acid ($H_2C_2O_4$) or oxalate ($C_2O_4^{2-}$) in alkaline solution, methane (CH_4), ethylene (CH_2CH_2), or ethanol (CH_3CH_2OH).[68,69]

Table 2. CO_2RR into various products and their thermodynamic potentials.

Reaction	Thermodynamic potential (E_0, V vs RHE)
$CO_2 + 2H^+ + 2e^- \rightarrow CO + H_2O$	−0.11
$CO_2 + 2H^+ + 2e^- \rightarrow HCOOH$	−0.20
$CO_2 + 4H^+ + 4e^- \rightarrow HCHO + H_2O$	−0.07
$CO_2 + 6H^+ + 6e^- \rightarrow CH_3OH + H_2O$	+0.03
$CO_2 + 8H^+ + 8e^- \rightarrow CH_4 + 2H_2O$	+0.17
$2CO_2 + 12H^+ + 12e^- \rightarrow C_2H_4 + 4H_2O$	+0.06
$2CO_2 + 12H^+ + 12e^- \rightarrow C_2H_5OH + 3H_2O$	+0.08

In addition, different catalysts often exhibit different CO_2RR mechanisms.[70] The thermodynamic electrochemical half-reactions of the CO_2RR and their associated standard electrode potentials are listed in **Table 2**.[69–71]

The selectivity of the CO_2RR toward the synthesis of particular products is also an important factor to evaluate the electrocatalytic performance.[72] Several approaches for optimizing the selectivity of the CO_2RR have been reported, including: 1) a precise control of crystal facets and defects for metal-based materials; 2) a modulation of the electronic and structural properties of single metal atoms in the metal alloys and SAECs; 3) a fine-tuning of the microstructures of catalytic supports including the carbon-based materials. SAECs show a great promise for the CO_2RR due to their tunable activity and high selectivity.[6,71] The binding strength of intermediate species over catalytic sites determines the yield of final products. In terms of energy density and industrial demand, the production of C_n ($n \geq 2$) hydrocarbons via CO_2RR is highly desirable.[73–75] For example, ethylene can be used for producing polyethylene, ethylene oxide, and diesel. Ethanol is also an important feedstock for ethane, glycol ethers and a renewable liquid fuel. Unfortunately, the weaker bond energy of C—C compared to H—H and C—H bonds generally disfavors the C—C coupling to form C_2 and C_n ($n > 2$) compounds.[76,77] Despite a rapid progress in this field, the development of novel SAECs for highly-efficient conversion of CO_2 into value-added hydrocarbon compounds still remains a grand challenge.

It is worth noting that the electrochemical reduction of CO_2 to CH_4 has a thermodynamic potential of +0.17 V versus RHE. However, CO_2 reduction usually requires extra energy to drive because of the chemical inertness of CO_2 and its sluggish reaction kinetics.[73,78] Therefore, CO_2RR is often carried out in the negative potential range (vs RHE) to obtain certain desired products. Similar to the NRR, the CO_2RR also competes with the HER at all negative potentials. Because of this, a key criterion for a superior CO_2RR catalyst is to suppress the HER activity in the presence of CO_2. Therefore, a common strategy for the improvement of the efficiency of CO_2RR is to regulate the ΔG_{H*} away from zero so to suppress HER activity.[79] To achieve a high selectivity for the synthesis of hydrocarbons in the CO_2RR, catalytic systems should offer both a moderate negative ΔG_{H*} away from zero and a high efficiency for CO_2 activation.

2.6. Other Electrochemical Reactions

The fuel oxidation including hydrogen, formic acid, methanol, and ethanol occurs at the anode of fuel cell devices to generate chemical energies.[80,81] Precious metal-based catalysts (Pt, Pd, Au, Ir, and their alloys) exhibit excellent electrocatalytic properties for these oxidation reactions due to their moderate adsorption energies for reactants/intermediates. The oxidation reaction of carbon-containing fuels often involves the generation of several intermediate C species over the catalyst surface. These intermediate species potentially block the limited sites for the further adsorption of fuel compounds, leading to slower electrooxidation kinetics.[80–82] For example, a partial electrochemical oxidation of methanol often occurs to produce various intermediate species including COH*, HCHO*, and CO* adsorbed strongly on the catalyst surface. These intermediates can block the active sites for further adsorption of methanol, thus decreasing the overall efficiency of electrochemical oxidation process.[82] Similar to the CO_2RR, the anodic oxidation of fuels involves a multiple-electron transfer with complicated mechanisms.[83–85] In addition, the precious metal catalysts are more vulnerable to poison by intermediates during oxidation process. The current challenge for the electrochemical oxidation of fuels is to develop efficient and robust catalysts with a high metal utilization and high tolerance to CO-based species. Recently, several precious metal-based SAECs have been reported as efficient fuel oxidation electrocatalysts,[86–88] which will be described in detail in following sections.

3. Engineering the First Coordination Sphere

Metal atoms in SAECs are stabilized by chemical bonding with an appropriate host material. The atomic architecture of the coordination site, defined by the number, chemical identity, and arrangement of nearest neighbor atoms as well as their extended local environment, determines the geometric and electronic structure of a SAEC, and its associated catalytic properties. The coordination number of the metal reflects the number of host atoms to which it is bonded, while the geometry depends on their arrangement. The specific interaction of the metal with the host can be controlled by tailoring these properties.[5,10,11,13–15] This may result in unique electronic properties (e.g., charge/spin states, electron density near Fermi level (E_F)), distinct from those observed for metal nanoparticle counterparts.[5,10,13,89] In this section, we highlight recent efforts to engineer the first coordination sphere of various metal-based SAECs for remarkable electrocatalytic performance (**Figure 3**).

3.1. Coordination Number

Carbon-based materials are widely used as metal-free supports in the fabrication of SAECs due to their high specific surface area, electrical conductivity, tunable porous structure, and the versatility for chemical functionalization.[16–18,89] A wide range of carbon supports with different morphologies and compositions have been developed via different synthetic approaches including carbon nanotubes, graphene (G), graphdiyne, g-C_3N_4, and porous carbon substrates derived from metal organic frameworks or polymers.[16–18,89–104] Nitrogen doping is widely exploited to modify the interaction of metal atoms with carbon materials via the formation of M—N bonds.[16,89–91,101–105] For instance, three typical microstructures of single Fe atoms have been reported in carbon-based SAECs (**Figure 4**A).[106] Compared to Fe atoms coordinated to four pyrrolic N atoms (denoted as D2), the active site of Fe coordinated to four pyridinic N atoms (denoted as D1) exhibits a higher ORR activity due to its optimized adsorption energies of the OH* intermediate during the ORR. This is supported by the observation of a high redox peak intensity of Fe^{2+}/Fe^{3+} at ≈0.75 V versus RHE and the detailed structural characterization by in situ

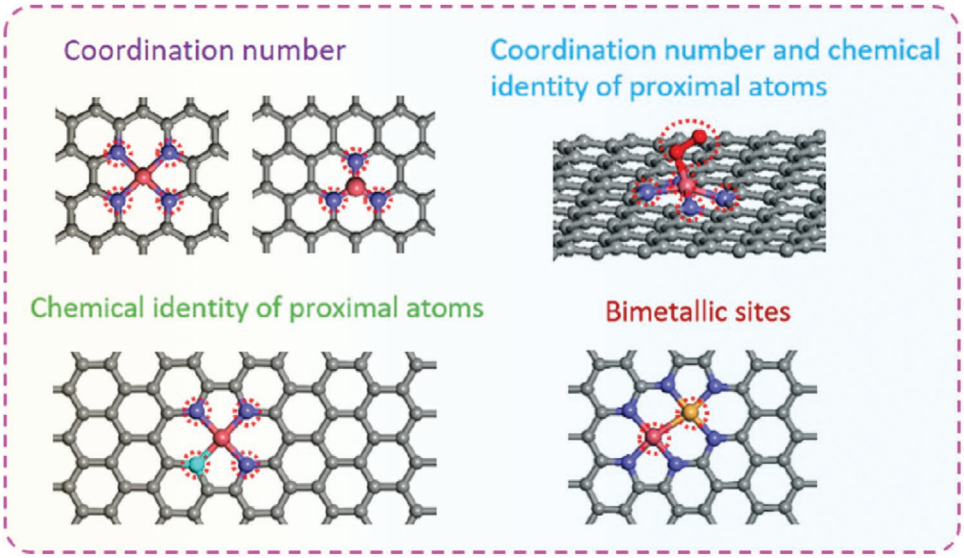

Figure 3. Engineering the first coordination sphere of SAECs, including variation of the coordination number, chemical identify of proximal atoms and the construction of bimetallic sites.

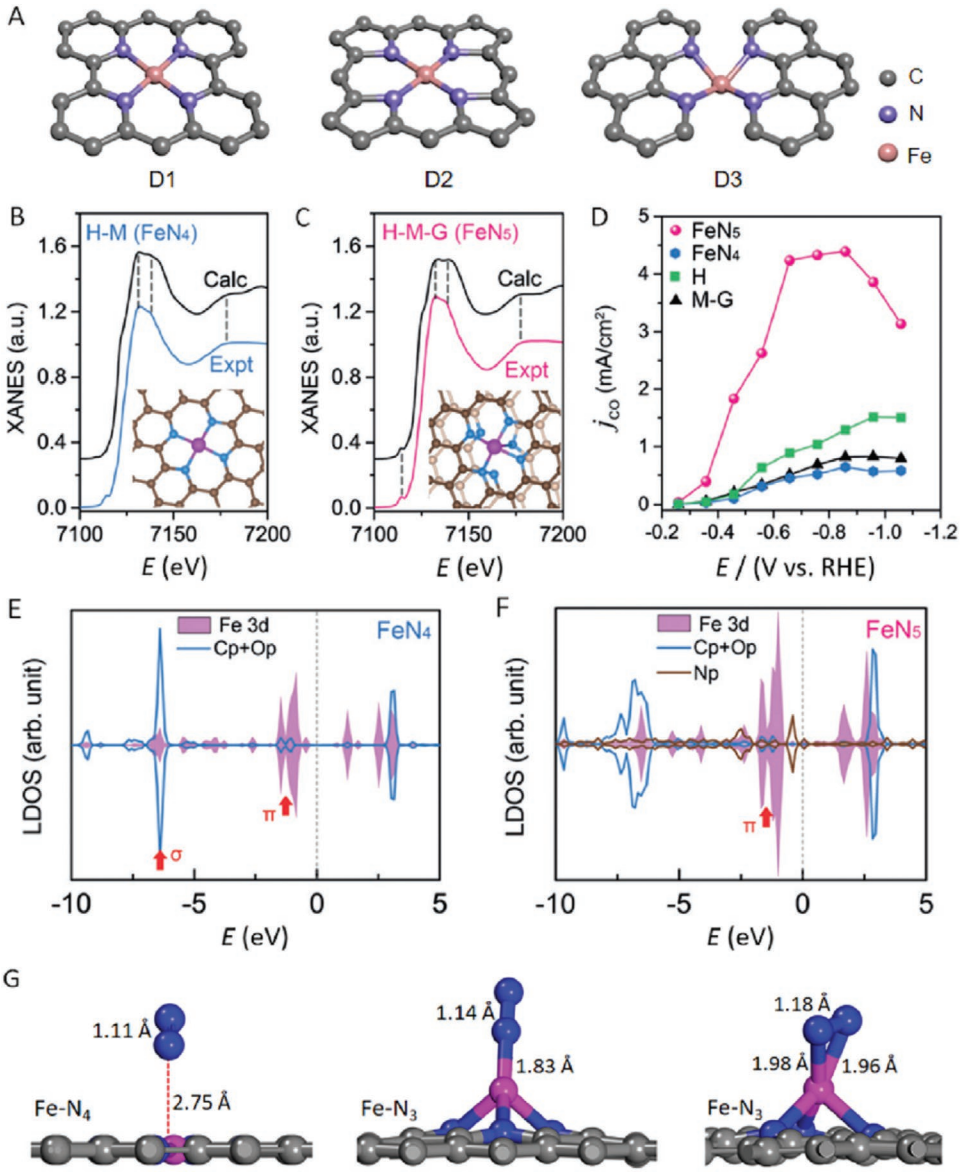

Figure 4. A) Three typical atomic structures of Fe_1-SAECs. Fe coordinated to four pyridinic N atoms (left). Fe coordinated to four pyrrolic N atoms (middle). Fe coordinated to four pyridinic N atoms embedded in microporous carbon materials (right). B,C) Experimental and simulated Fe K-edge XANES data of FeN_4 (derived from the pyrolysis of hemin and melamine, H–M) and FeN_5 (derived from the pyrolysis of hemin and melamine on graphene, H–M–G). The insets show the DFT-optimized structures of FeN_4 and FeN_5, respectively. D) Partial current densities on CO during CO_2RR. E) LDOS of the FeN_4 and F) FeN_5 system with adsorbed CO; zero-energy corresponds to the Fermi level of individual systems. G) Optimized structures of N_2 adsorption over Fe–N_4 sites and Fe–N_3 sites. A) Reproduced with permission.[106] Copyright 2015, American Chemical Society. B–F) Reproduced with permission.[112] Copyright 2019, Wiley-VCH. G) Reproduced with permission.[120] Copyright 2019, American Chemical Society.

extended X-ray absorption fine spectroscopy (EXAFS) combined with ex situ Mössbauer spectroscopy.[106–108] In addition, it has also been demonstrated that the immobilization of Fe coordinated to four pyridinic N atoms in microporous carbon materials (denoted as D3) enhances the ORR kinetics to further improve the ORR performance with a large current density and high turn-over frequency.[109] The presence of a hydroxyl group as the axial ligand to Fe centers in D3 increases the valency of Fe and strengthens the interaction between Fe atoms and oxygen intermediates, which can efficiently lower the energy barrier of OH* desorption from active sites in both acidic and alkaline media as revealed by density functional theory (DFT) calculations.[110,111] Such an electronic hybridization between metal and proximal atoms often results in the modification of the near-Fermi DOS and charge state of the metal attributed to the enhanced catalytic performances. For instance, the coordination number of Ru atoms supported on N-doped carbon is determined to be 3.4 ± 0.4, which is much lower than that of Ru nanoparticles (7.3 ± 0.4). The lower coordination number of Ru in the Ru_1-SAEC facilitates the dissociation of chemically inert N≡N* bonds and leads to enhanced N_2 activation compared with Ru nanoparticles, which is responsible

for the excellent NRR activity with a high yield of 120.9 μg_{NH3} $mg^{-1}_{cat.}$ h^{-1}.[102]

To date, numerous SAECs with M−N_x active centers have been reported to display superior electrocatalytic activities to metal nanoparticles. The interaction can be tailored by varying the number of nearest N atoms. Recently, we prepared Fe_1-SAECs containing the FeN_5 center supported on N-doped graphene (NG) through the thermal pyrolysis of hemin (H) and melamine (M) coadsorbed on graphene.[112] FeN_5 sites can be constructed via the coordination of a FeN_4 site with an additional axial ligand from N-doped graphene. Fe_1-SAECs with FeN_4 and FeN_5 centers can be obtained through the prolonged thermal pyrolysis of different precursors, as evidenced by X-ray absorption near-edge structure (XANES) in combination with other techniques (Figure 4B,C). Among all the synthesized catalysts, FeN_5-SAEC exhibits the highest partial current density for the electrochemical reduction of CO_2 into CO in the range of −0.26 to −1.06 V versus RHE, much higher than that of FeN_4-SAEC (Figure 4D). The calculated free-energy change of one key-step ($CO_2 \rightarrow$ *COOH) over the FeN_5 catalyst is 0.77 eV, significantly lower than that over the FeN_4 catalyst (1.35 eV). Therefore, the FeN_5 catalyst exhibits excellent activity for CO_2RR into CO, superior to the FeN_4 catalyst. Detailed analysis of the DOS and partial charge density of the two active sites with CO adsorption (CO_FeN_4, CO_FeN_5) reveals that the σ bonding interaction between CO and Fe of FeN_4 (located around −6.4 eV) arises from the d_z^2 orbital of Fe and the p_z orbitals of C and O (Figure 4E). On the other hand, the CO 2π* coupling to Fe 3d states gives rise to new bonding states below E_F. Due to the p–d coupling between pyrrolic N and Fe in FeN_5, the bonding states between N and FeN_5 (N_FeN_5) are distributed in the range from −3.31 to −1.92 eV, much lower than that of CO_FeN_5 (from −1.80 to −0.99 eV). Bader charge analysis suggests a higher oxidation state of Fe in FeN_5 (+1.19 e) than in FeN_4 (+0.98 e). The difference is attributed to the d electron transfer from Fe to the p_x and p_y orbitals of the pyrrolic N atom, which can efficiently reduce the Fe−CO π back-donation (Figure 4F) and thus weaken the CO adsorption strength and enhance the selectivity for CO production over the FeN_5 centers. This work together with a previous study on CoN_5-SAEC demonstrates that high selectivity of CO_2RR toward certain product can be achieved by tuning the coordination number of individual metal atoms.[113]

Although FeN_4 has proven to be an excellent active site for ORR, HER, OER, and CO_2RR,[14,16,18,79,114–119] it is catalytically inactive for nitrogen reduction.[120] As described in Section 2.4, N_2 adsorption and activation (N≡N*) are critical steps for the NRR. Single Fe atoms bonded with three pyridine-N atoms (FeN_3) activate N_2 more effectively than Fe in FeN_4 (four pyridine-N atoms), as evidenced by the increased N≡N bond length from 1.11 to 1.14 or 1.18 Å estimated from the stretching frequency (Figure 4G), and thus facilitate the chemisorption of N≡N* in the NRR. Because of this, FeN_3-SAEC exhibits the highest NRR activity (a rate of 34.83 μg h^{-1} $mg^{-1}_{cat.}$ at a low voltage of −0.2 V vs RHE) among all nonprecious metal-based SAECs.[120] Optimization of the performance of SAECs by tuning the coordination number has also been demonstrated in Cu_1-SAECs for ORR and CO_2RR.[121–123] It is found that CuN_2 with a valence state of ≈1.22 facilitates the O_2* adsorption with a strong chemical interaction, while CuN_4 with a valence state of ≈2.0 shows a higher free energy for O_2* adsorption during ORR. Analysis of the projected DOS (PDOS) revealed new hybridized electronic states above E_F upon the adsorption of one O atom on CuN_2. This reduces the occupation of antibonding states of O−CuN_2, resulting in a stronger O−Cu bonding for CuN_2 as opposed to CuN_4 and CuPc molecule, while is weaker than that of CuN_3.[121] Therefore, the Cu–N_2 structure offers an intermediate binding strength with the O species responsible for the enhanced ORR catalytic activity.

Precious metal catalysts have been widely used for electrochemical conversions. However, their high cost and potential catalyst poisoning by some intermediate species or impurities have greatly restricted the applications.[9,124] For instance, Pt nanoparticles are easily poisoned by CO/methanol due to their strong binding affinity for these molecules, which leads to inefficient performance in the hydrogen oxidation reaction (HOR), and the oxidation reaction of carbon-containing fuels.[80,82] In contrast, isolated Pt atoms on metal supports present a high tolerance to CO and high activity for the oxidation reaction of carbon-containing fuels,[125–127] such as the formic acid oxidation (FAO) reaction.[125] In a recent study, the coordination number of a single Pt atom in PtAu nanoparticles could be regulated from five to nine by controlling the metal ratio.[125] Isolated Pt atoms in Pt_4Au_{96} with the lowest coordination number were most active in FAO, exhibiting a current density at ≈0.6 V versus RHE in the anodic sweep, 126 and 90 times higher than those of $Pt_{78}Au_{22}$ and Pt/C catalysts, respectively (**Figure 5**A). A ratio of Pt/Au lower than 17:83 generally produces atomically dispersed Pt in bimetallic PtAu nanoparticles as revealed by a combination of X-ray photoelectron spectroscopy (XPS) and extended X-ray absorption fine structure (EXAFS) measurements. An increase of the Pt/Au ratio (53:47) tends to form Pt clusters with an increased Pt-Pt coordination number in the alloyed nanoparticles (Figure 5B). A significant peak is observed at ≈0.85 V versus RHE in the CV plot for $Pt_{53}Au_{47}$, $Pt_{78}Au_{22}$, and Pt/C, which arises from the electrochemical oxidation of CO molecules during the reaction (i.e., poisoning the surface of Pt). This result demonstrates that the coordination number of precious metals is strongly correlated with their tolerance to poisoning. The excellent FAO performance of Pt_4Au_{96} is attributed to the weakened adsorption of CO over the single-atom Pt site as supported by the disappearance of the peak at 0.85 V versus RHE in the FAO forward sweep, which is different from Pt clusters on $Pt_{53}Au_{47}$ nanoparticles. The adsorption energy of CO over single Pt atoms is calculated to be −1.032 eV, which is lower than that of CO over a few-atoms (−1.063 eV) or bulk Pt (−1.268 eV), respectively (Figure 5C,D). This leads to the excellent FAO activity of Pt SAECs (a high forward current density of 3.77 A mg_{Pt}^{-1} and high tolerance to CO on Pt_4Au_{96}). Improvements in the electrocatalytic performance upon reducing the coordination number have also been demonstrated for Pt_1-SAECs on antimony-doped tin oxide (ATO) with high FAO activity and excellent tolerance to methanol.[128] In this case, Pt atom is immobilized on the support via the formation of Pt−Sn and Pt−O bonds with an average Pt coordination number of ≈3.4, much lower than that of Pt foil (12). As described in Section 2.6, the MOR process involves a six-electron process

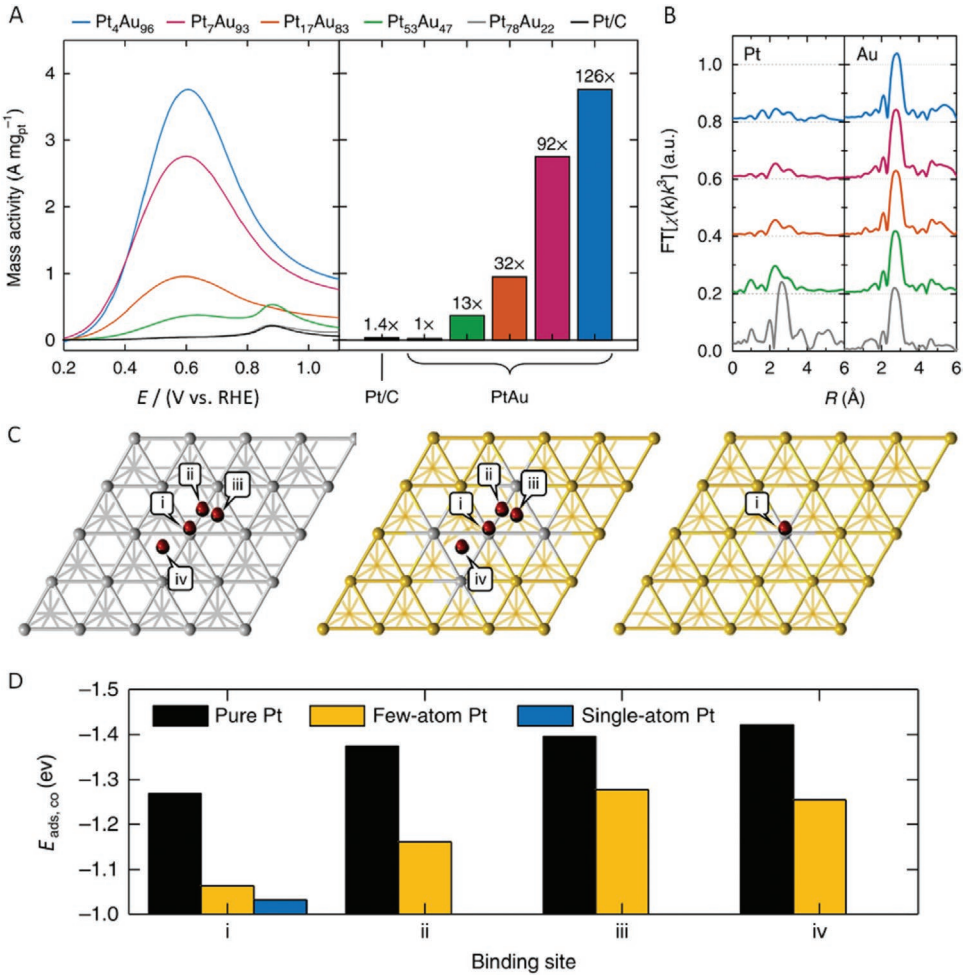

Figure 5. A) Pt mass-normalized anodic sweeps obtained from PtAu nanoparticle catalysts in an electrolyte containing both $HClO_4$ and HCOOH (0.1 M). The peak currents are graphed for comparison (left). The data acquired for a commercial Pt/C catalyst is also included. B) Fourier transform of k_3-weighted Pt and Au L_3-edge EXAFS spectra of a series of PtAu nanoparticles. The color-coded curves correspond to $Pt_{78}Au_{22}$, $Pt_{53}Au_{47}$, $Pt_{17}Au_{83}$, Pt_7Au_{93}, and Pt_4Au_{96} from bottom to top, respectively. C) Structural models of CO adsorption on the clean (left), few-atom (middle), and single-atom (right) modified Pt (111) surfaces, identifying distinct coordination sites including i) apical, ii) bridging, iii) hexagonal close-packed hollow, and iv) face-centered cubic hollow. D) Calculated adsorption energies for the indicated CO adsorption sites. A–D) Reproduced with permission.[125] Copyright 2018, Nature Research.

with complicated oxidation mechanisms. The COH* formation from CH_3OH (the first step in MOR) is not favorable over the single Pt atom,[82,129] leading to excellent tolerance to methanol.[125–128] Engineering the coordination number of precious metal centers has the potential not only to enhance their catalytic activity and selectivity, but also to greatly improves their tolerance to poisoning.

3.2. Chemical Identity of Proximal Atoms

Atomically dispersed metals often form chemical bonds with host atoms of distinct chemical identity, such as RuC_2N_2 for HER,[130] CoC_2N_2 for ORR,[131] CoC_3N for HER,[132] $NiCN_3$ for CO_2RR,[133] and SnC_2N_2 for CO_2 reduction into formate.[134] The ratio of nearest C/N atoms in these SAECs can be readily tuned by controlling the pyrolysis temperature, enabling optimization of their electrocatalytic activity.[130–132,135–137] For instance, Co atoms coordinated with three C and one N (CoC_3N) exhibit a high density of states in the vicinity of E_F, resulting in a moderate ΔG_{H*} to promote the overall HER, which differs from the strong H adsorption on CoN_4 and weak adsorption on CoC_4.[132]

The electron density of metal d orbitals near E_F can be regulated by tuning the coordination with C and N atoms due to their different electronegativities. A high DOS of a metal atom around E_F generally facilitates electron transfer and enhances the catalytic performance, as demonstrated in the single-atom Co for ORR and HER[131,132] and the cases of Mo and W for HER.[138,139] Chen et al. prepared a series of Ru_1-SAECs with different C/N ratios through tuning the pyrolysis temperature as shown in **Figure 6**.[130] RuC_2N_2 shows a much smaller $|\Delta G_{H*}|$ value than RuC_4 and RuN_4 (Figure 6A). In addition, the formation energy of RuC_2N_2 is higher than that of RuN_4 while lower than that of RuC_4. Therefore, the ratio of C/N bonded to a single

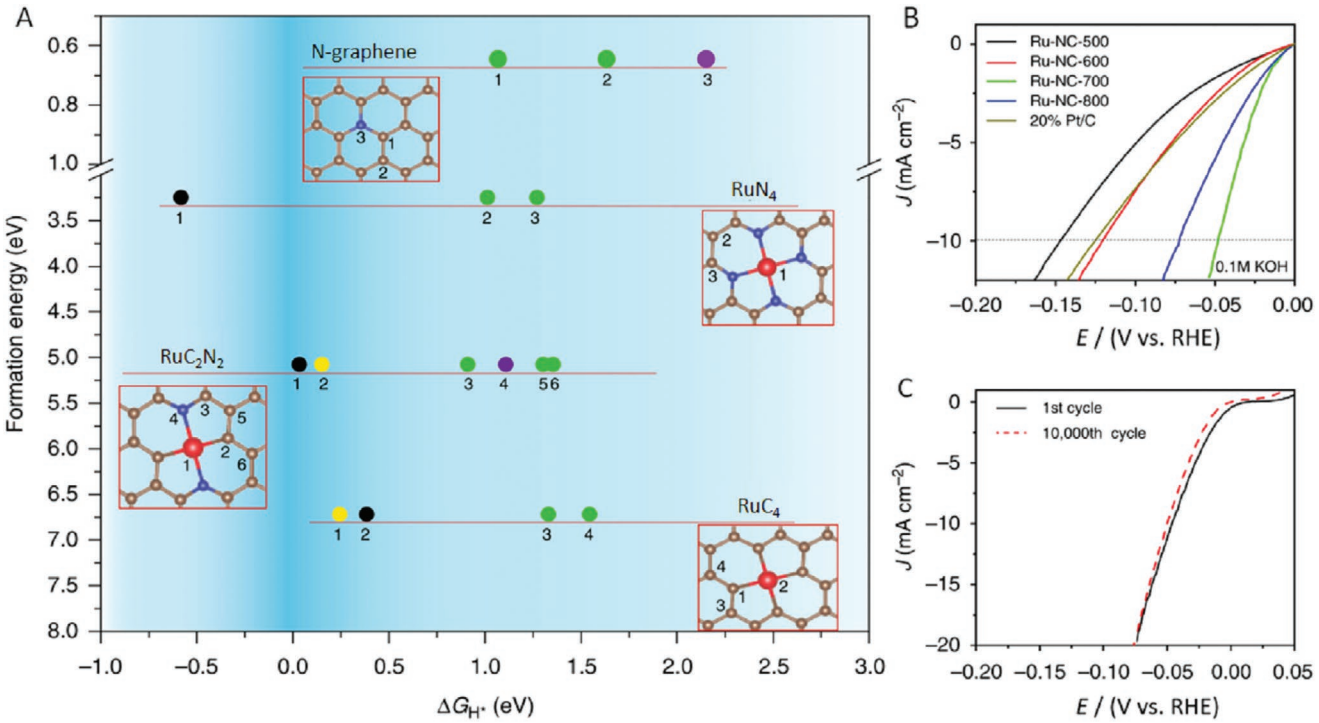

Figure 6. A) First principle calculations of the energy diagram of N-graphene, RuN_4, RuC_2N_2, and RuC_4 structures for HER. The *x* axis is the reaction free energy of hydrogen binding, and the *y* axis is the formation energy of each configuration. B) LSV curves of Ru-NC-T compared to that of commercial 20 wt% Pt/C in 0.1 M KOH. C) Stability test of Ru-NC-700 in 0.1 M KOH, before and after 10 000 cycles within the potential window of –0.05 to +0.05 V versus RHE. A–C) Reproduced with permission.[130] Copyright 2019, Nature Research.

Ru atom can be tuned by controlling the pyrolysis temperature. RuC_2N_2 center prepared at 700 °C exhibits the best HER activity (overpotential of 46 mV at 10 mA cm^{-2}) among the series of Ru_1-SAECs, as well as a robust stability after 10 000 cycles (Figure 6B,C).

Recently, several host materials containing distinct elements have been fabricated to control the chemical identity of atoms bonded to isolated metal centers such as $CoBN_3$,[140] $CoPN_3$,[141] $CuSN_3$,[142] MnS_2N_2,[143] $CoSN_3$,[144] and $FePN_3$[145] and evaluate the impact on the reactivity. The ORR performance of the CoN_4 site differs dramatically once one proximal N atom is replaced by B ($CoBN_3$). The introduction of B atoms into the carbon matrix to form a unique $CoBN_3$ center can create the unbalanced charge distribution around the metal center, positively polarizing the C atoms and Co–N–C sites, which beneficially favors the adsorption of oxygen species.[140] All these results demonstrate that engineering the ratio of different nonmetal atoms with different electronegativities provides an efficient method for improving the electrocatalytic activity of SAECs.

3.3. Coordination Number and Chemical Identity of Proximal Atoms

As described in Sections 3.1 and 3.2, both the coordination number and the chemical identity of proximal atoms determine the performance of SAECs. In many cases, simultaneously tuning these two factors permits optimization of the electronic state of single metal atoms and consequently the electrocatalytic performance.[104,146–149] For instance, the graphdiyne-supported Pt_1-SAEC consisting of a four-coordinated C_2–Pt–Cl_2 active site shows the best HER performance with an outstanding mass activity of 23.64 A mg_{Pt}^{-1} at an overpotential of 100 mV, 3.3 and 26.9 times higher than that of SAECs with a five-coordinated C–Pt–Cl_4 active site and commercial Pt/C catalysts, respectively.[104] Compared to the C–Pt–Cl_4 unit, a reduction in the strength of the Pt—Cl bond in the C_2–Pt–Cl_2 site increases the unoccupied DOS of Pt 5d orbital, favoring its hybridization with the 1s orbital of H atom. Additionally, C_2–Pt–Cl_2 shows a low $|\Delta G_{H^*}|$ of 0.092 eV for hydrogen adsorption, much lower than that of C–Pt–Cl_4 (0.653 eV). All these factors facilitate the electron transfer to H atoms for efficient electrochemical H_2 production.

Tour and co-workers synthesized Ru_1-SAECs supported by N-doped graphene via the thermal annealing of graphene oxide (GO) mixed with a trace amount of Ru salt ($Ru(NH_3)_6Cl_3$) under an NH_3 atmosphere.[146] Quantitative analysis by EXAFS and XANES revealed that Ru_1-SAEC contains a Ru–N_4 unit with axial oxygen adsorption (Ru-oxo-N_4), which is responsible for the ORR catalytic activity in acidic medium (**Figure 7**A). The chemical interactions of O_2* with Ru–N_4 is much stronger than Ru–N_4–O, leading to a high reaction barrier for the formation of OOH* (a large overpotential as evidenced in the evaluation of ORR performance, Figure 7B). Compared to Ru–N_4, Ru-oxo-N_4 with a higher metal oxidation state shows a positive shift of free energies between the reaction intermediates, facilitating the ORR. Introducing an electron-withdrawing nonmetal element adjacent to the single-metal active center

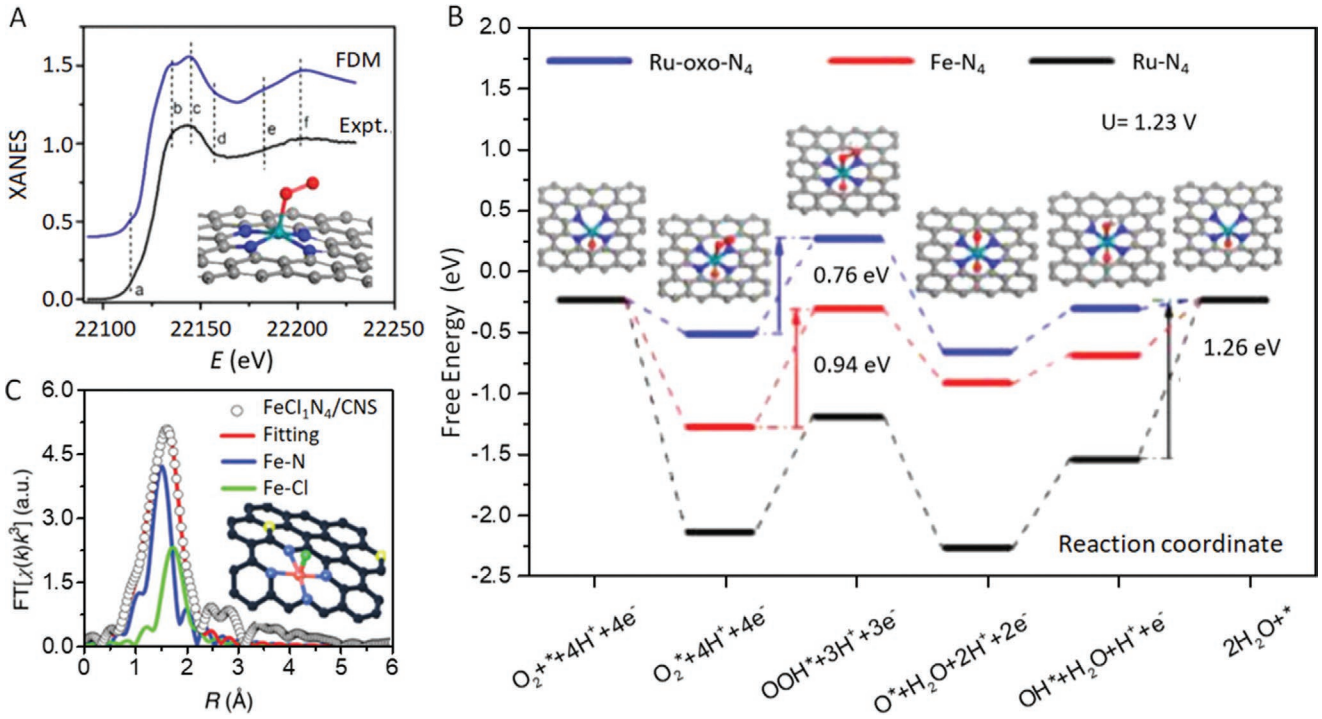

Figure 7. A) Experimental and simulated Ru K-edge XANES spectrum of Ru-N/G-750 (the theoretical spectrum corresponds to the calculated atomic model of Ru-N/G-750 shown inset). B) Free-energy diagram of the ORR catalyzed by selected nitrogen-coordinated metal moieties embedded in graphene. The proposed associative mechanism involves the following steps: 1) $O_2 + * \rightarrow O_2*$; 2) $O_2* + H^+ + e^- \rightarrow OOH*$; 3) $OOH* + H^+ + e^- \rightarrow O* + H_2O$; 4) $O* + H^+ + e^- \rightarrow OH*$; and 5) $OH* + H^+ + e^- \rightarrow H_2O$, where * denotes the adsorption site on the catalyst surface. C) The corresponding EXAFS fitting curves of the $FeCl_1N_4$/CNS in R space. A,B) Reproduced with permission.[146] Copyright 2017, American Chemical Society. C) Reproduced with permission.[147] Copyright 2018, Royal Society of Chemistry.

has been used for tuning the electronic states of the single metal atom.[147] Wang et al. have prepared Fe_1-SAECs by pyrolyzing a mixture of chloride salts (NaCl and KCl) and polymers containing Fe and N atoms.[147] The as-synthesized Fe_1-SAEC exhibits an outstanding ORR activity with a half-wave potential ($E_{1/2}$) of 0.921 V versus RHE, much higher than that of Pt/C ($E_{1/2}$ = 0.842 V vs RHE). EXAFS data suggest that the iron atom in Fe_1-SAECs is coordinated with a Cl atom (at 2.19 Å) and four N atoms (1.92 Å) (Figure 7C). Theoretical calculations reveal that the iron atom in $FeClN_4$ has a broader d band close to E_F than that of Fe in FeN_4, which leads to a weaker binding energy of O_2 over $FeClN_4$ than that of FeN_4 and thus facilitates the desorption of OH* species over $FeClN_4$. Other examples that illustrate how the electronic properties of SAECs can be modulated by changing the adjacent coordination number and ratio of proximal atoms for improved ORR efficiency include single Fe atom coordinated by four N atoms and one P atom,[148] and single Pt atom coordinated by two S atoms and two water molecules.[150]

The selectivity of CO_2RR toward the synthesis of particular products is an important factor to evaluate the electrocatalytic performance of SAECs. Very recently, Zhang and coworkers prepared a series of Mn_1-SAECs containing MnN_4 sites and proximal halogen atom (Cl, Rr, I) for improving CO selectivity in CO_2RR (**Figure 8**).[149] The standard EXAFS fitting reveals that a single Mn atom is coordinated with a Cl atom and four N atoms ((Cl, N)–Mn/G) (Figure 8A). Due to a strong electron-withdrawing effect of Cl, the bond length of Mn–N in Mn_1-SAECs is elongated from 2.02 Å (N–Mn/G) to 2.08 Å, resulting in an out-of-plane distortion of the metal atom. $MnClN_4$ exhibits an excellent CO_2RR performance including a large current density of CO_2RR and high FE_{CO} (Figure 8B,C), superior to these catalysts without Cl coordination. Interestingly, $MnClN_4$ offers a higher FE_{CO} value up to 97%, compared to $MnBrN_4$ (92%) and $MnlN_4$ (89%). The free energy profiles of CO_2RR catalyzed by (Cl, N)–Mn/G and N–Mn/G is shown in Figure 8D. At the potential of $U = 0$ and –1 V versus RHE, the reaction step for CO* to CO over $MnClN_4$ with a lower ΔG can proceed more easily than that over MnN_4, indicating that the $MnClN_4$ center is more favorable for CO_2RR into CO. The calculated free energy for H* adsorption on $MnClN_4$ is 0.92 eV, much higher than that of MnN_4 (0.11 eV), suggesting that the HER is significantly suppressed over $MnClN_4$ (Figure 8E). The calculated d-band center of $MnClN_4$ shows a downshift of 0.38 eV upon the interaction with COOH*, much larger than that in MnN_4 (0.12 eV) (Figure 8F). This result suggests Cl coordination to MnN_4 facilitates the electron transfer between COOH* and $MnClN_4$. Therefore, MnN_4 coordinated with Cl exhibits a high selectivity toward CO production in CO_2RR.

3.4. Bimetallic Sites (M1–M2)

Bimetallic SAECs consisting of two adjacent nonprecious single metal sites (M1–M2) can show a higher electrocatalytic

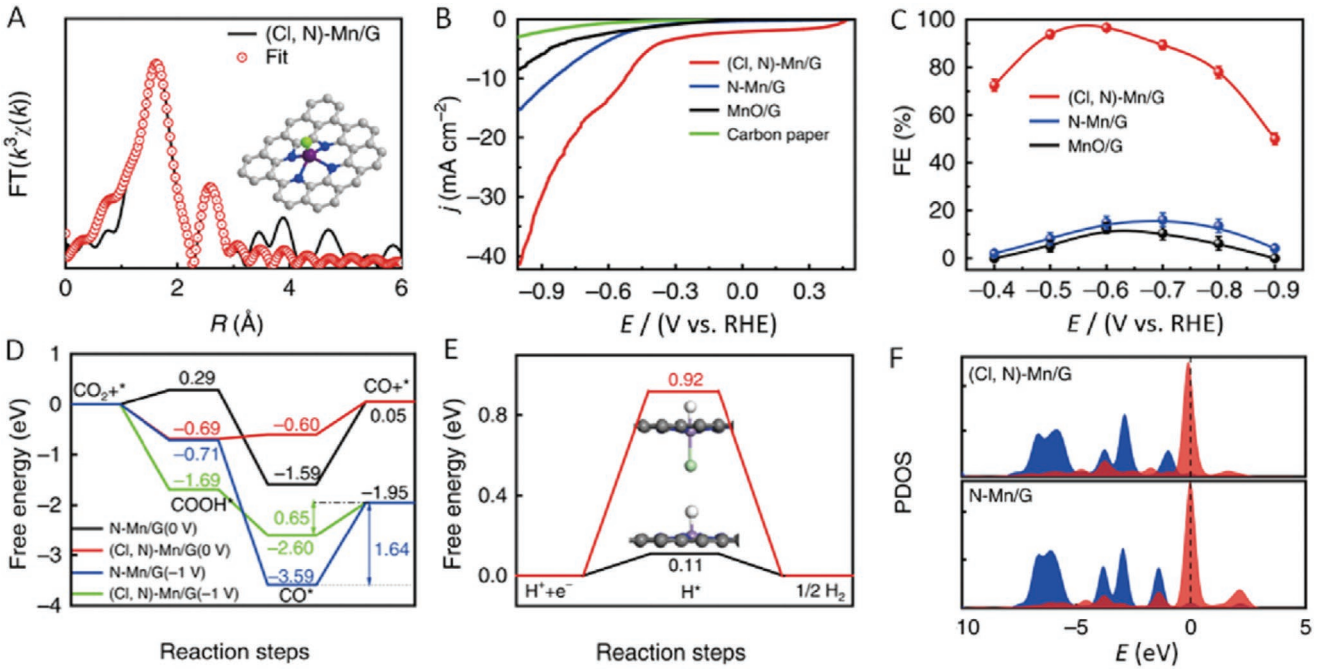

Figure 8. A) EXAFS fits of the (Cl,N)–Mn/G with $MnClN_4$ center in R space. The inset illustrates the atomic model of (Cl,N)–Mn/G. B) LSV curves of different catalysts (in a CO_2-saturated 0.5 M $KHCO_3$ solution, scanning rate: 10 mV s^{-1}). C) FE_{CO} at various applied potentials. D) Calculated free energies of CO_2RR. E) Calculated free energies of hydrogen adsorption. F) Projected DOS of the COOH* 2p state (blue-shaded areas) and d-projected DOS of Mn (red-shaded areas) in the adsorption structures for (Cl, N)–Mn/G and N–Mn/G (MnN_4 site), respectively. A–F) Reproduced with permission.[149] Copyright 2019, Nature Research.

performance compared to monometallic SAECs and commercial Pt/C catalysts, such as Co–Fe,[151–153] Fe–Ni,[154] Zn–Co,[155] Ni–Co,[156] and Pt–Ru.[157] The immobilization of two adjacent single metal atoms in carbon-based materials can greatly reduce the barriers of the key reaction steps in electrocatalysis. For instance, the active site containing a dual Fe–Co center bonded with six N atoms on N doped porous carbon support possesses a high activity for ORR (**Figure 9**A–D).[152] This bimetallic Fe_1Co_1-SAEC catalyses the dissociation of O_2 and OOH* into O* and OH* with a lower energy barrier than that of monometallic Fe_1- and Co_1-SAECs. The low dissociation barrier was attributed to the strong binding of O_2 to the Fe–Co dual site with a significant elongation of O—O bond from 1.23 Å (gas-phase) to 1.40 Å.[151] The maximum external potential at which the ORR process is exothermic, can be treated as the limiting potential (U_{lim}). Fe atoms in the dual Fe–Co sites are predicted to show a remarkably high U_{lim} (0.99 V vs RHE), superior to single Co-based SAECs (0.67 V vs RHE), Pt (0.79 V vs RHE), and the Co atom (0.82 V vs RHE) in the Fe–Co dual center.[152] In addition, reaction intermediates over the Fe–Co dual center show different adsorption behaviors compared to single-metal centers (Figure 9E,F). In the former case, two metal sites participate in the chemical adsorption of intermediates, which also favors the dissociation of OOH* into OH* and O* species. Similarly, the incorporation of dual metal sites for the regulation of their overall catalytic activity is also demonstrated in other bimetallic SAECs.[154–156] The ORR overpotential catalyzed by a dual Zn-Co SAEC is determined to be 0.335 V versus RHE under alkaline conditions, superior to that of ZnN_4 (0.436 V vs RHE) and CoN_4 (0.391 V vs RHE).[155] The dual Zn–Co bimetallic center also exhibits a higher O_2 activation with an increased O—O bond length compared to single metal centers.

Monometallic Fe_1 and Co_1-SAECs have been widely employed for ORR. Unfortunately, their performance toward the reverse OER is unsatisfactory, leading to a big challenge for their application as bifunctional ORR/OER catalysts.[158] Bimetallic Ni_1Co_1-SAECs consisting of a dual Co–Ni center with a single Ni atom bonded to a Co atom exhibits excellent performance for both ORR and OER.[156] The measured overpotential for the OER at 10 mA cm^{-2} over Ni_1Co_1-SAECs (≈340 mV) is lower than over CoNi nanoparticles (440 mV), N doped carbon (NC, 745 mV), or commercial IrO_2 (400 mV). Moreover, bimetallic Ni_1Co_1-SAEC also exhibits a promising ORR performance including a high onset potential (E_{on} = 0.88 V vs RHE) and large current density (4.95 mA cm^{-2}), comparable to commercial Pt/C (E_{on} = 0.90 V vs RHE, 5.09 mA cm^{-2}). At U = 0 V versus RHE, the downhill free energy pathways in the ORR manifest that all electron transfer steps are exothermic over NC, Ni_1-SAECs, and Ni_1Co_1-SAECs. At a potential of 1.23 V versus RHE, the hydrogenation of molecular O_2 acts as the limiting step with energy barriers of 1.09 and 0.63 eV over NC and Ni_1-SAECs, respectively. In addition, the largest uphill value further decreases to 0.35 eV for Ni_1Co_1-SAECs. As a result, the limiting step shifts to the protonation of OH*, pointing out the critical role of dual Ni–Co sites for the catalytic ORR process (Figure 9G). At U = 1.57 V versus RHE, the free energy profiles for OER over these SAECs are shown in Figure 9H. The adsorption of OH* is the limiting step with the energy barriers of 1.43 and 0.97 eV for NC and Ni_1-SAECs, respectively. It is found that Ni_1Co_1-SAEC can efficiently promote the reaction with a reduced energy barrier of 0.69 eV.

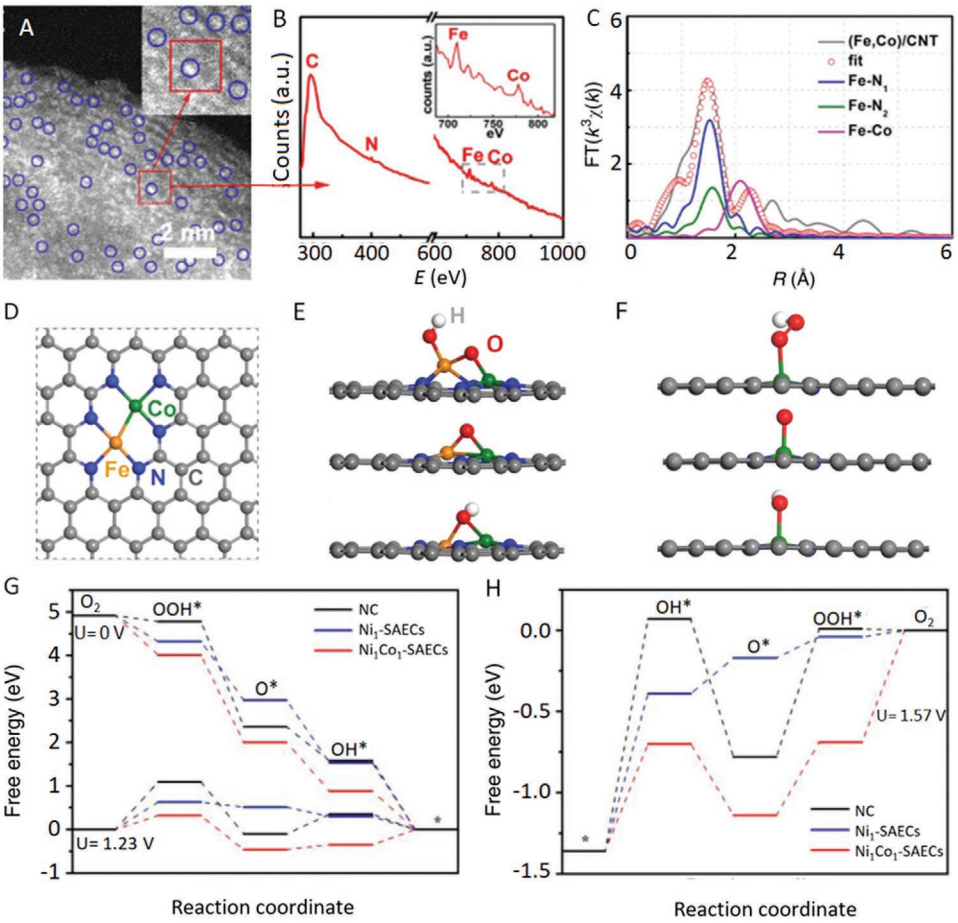

Figure 9. A) Magnified HAADF-STEM images of the dual atom Fe and Co sites imbedded in carbon materials. B) The electron energy-loss (EEL) spectrum was taken in the region marked by the red rectangle in (A). The coexistence of Fe, Co, N, and C indicates that Fe, Co are coordinated with N at the atomic scale. C) The corresponding Fe K-edge EXAFS fits of (Fe,Co)/CNT. D) The proposed architecture of dual Fe–Co sites. E,F) Geometric structures of the intermediates OOH*, O*, and OH* adsorbed on E) dual Fe–Co sites and F) Co single site. Calculated free energy diagram of G) ORR and H) OER processes on NC, Ni_1-SAECs, and Ni_1Co_1-SAECs. A–F) Reproduced with permission.[152] Copyright 2018, Royal Society of Chemistry. G,H) Reproduced with permission.[156] Copyright 2019, Wiley-VCH.

Because of all these figures of merits, a two-electrode Zn–air battery using Ni_1Co_1-SAECs as the cathode catalyst delivers a high-power density (101 mW cm^{-2}), unmatched by other catalysts. Therefore, engineering dual-metal site (M1–M2) in bimetallic SAECs offers another efficient approach to facilitate the key reaction step toward excellent electrocatalytic performance.

4. Engineering the Second Coordination Sphere and Beyond

Electronic structures of active sites in SAECs can be further optimized to enhance catalytic performance by tuning the second coordination sphere and beyond of single-metal center. The second coordination sphere and beyond refer to the atoms that are bonded to atoms in the first coordination sphere but not to the single-metal atom. Generally, three efficient approaches have been developed to realize this target. These include i) heteroatom doping into carbon frameworks, wherein heteroatoms are bonded with proximal atoms in the vicinity of the catalytic center; ii) engineering vacancy/edge near the active site; iii) constructing dual metal sites linked by a nonmetal atom (e.g., M1–O/N–M2, such as Fe–O–Pt,[159] Zn–N–Co[160]). In this section, we highlight recent efforts that exemplify the relevance of engineering the second for enhanced electrocatalytic performance (**Figure 10**).

4.1. S, P, B Heteroatom Doping

Heteroatom doping of carbon-supported MN_x-SAECs with other nonmetal elements such as B, S, and P can originate highly active sites for electrocatalytic applications. Heteroatoms outside the first coordination sphere can also influence the distribution of the electron density over single-metal active centers ($M–N_x/C$) and effectively tune their catalytic activity.[160–168] Among all the heteroatoms investigated, S has emerged as a highly effective nonmetal dopant.[160,161,163–166] Because of a lower electronegativity of S (2.58) compared to N (3.04), electron density shifts from S to N atoms when a S—N bond is formed.[161]

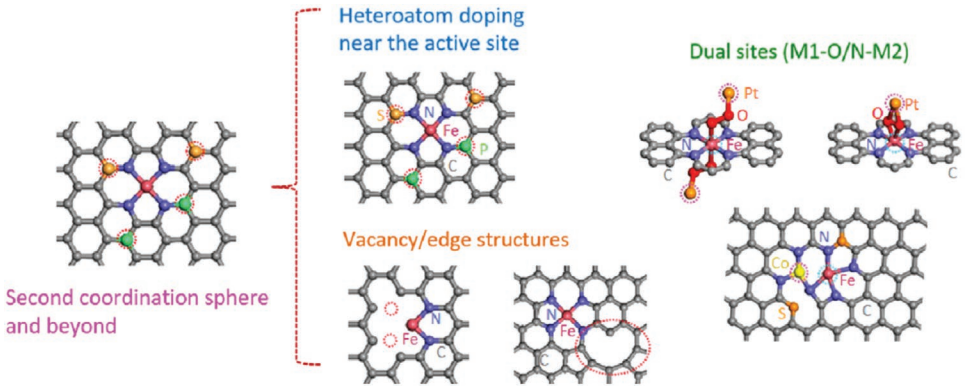

Figure 10. Engineering the second coordination sphere of SAECs and beyond, including heteroatom doping close to the isolated metal center, but not adjacent to the active site, the creation of vacancies and edges, and the construction of dual metal sites, which may be connected in different ways.

Further bonding of N with FeN_4 center increases the total electron density of the catalytic center, and thus facilitates the OH* desorption toward enhanced ORR efficiency under alkaline conditions (**Figure 11**). The EXAFS measurement reveals that FeN_4-SAEC upon S doping exhibits two types of Fe—N bonds with different lengths (1.86 and 1.97 Å), in contrast to FeN_4-SAEC with one set of Fe—N bonds (1.91 Å) (Figure 11A,B). This is because of a pair of S atoms bonded with two N atoms, resulting in an asymmetric distribution of the four Fe—N bonds in S, N codoped FeN_4-SAEC (Fe-ISA/SNC) (Figure 11B). In addition, the redistribution of electron density from S to adjacent N atoms creates a positive valence state (+1.2) of S as demonstrated by S K-edge XANES spectra (Figure 11C–E). Such a shift of electron density from S to N facilitates the OH* desorption responsible for the enhanced ORR activity (Figure 11F). In addition to S, the use of B and P dopants directly bonded with N can also tune the electronic structures and catalytic properties of Fe–N_4 centers. The charge density analysis of a P modified Fe–N_4 center shows that electron donation from an adjacent P atom lowers the positive charge of Fe ($Fe^{\delta+}$) in Fe_1-SAEC/NP-C, reducing the OH* binding energy, which is beneficial for its desorption over Fe sites in the ORR.[157] In contrast to S and P dopants with electron-donating properties, B bonded with N in FeN_4 behaves as an electron acceptor, resulting in a shift of electron density from N to B.[162,167] Such a charge redistribution alters the Fe d-band center crossing E_F. As a result, the reaction

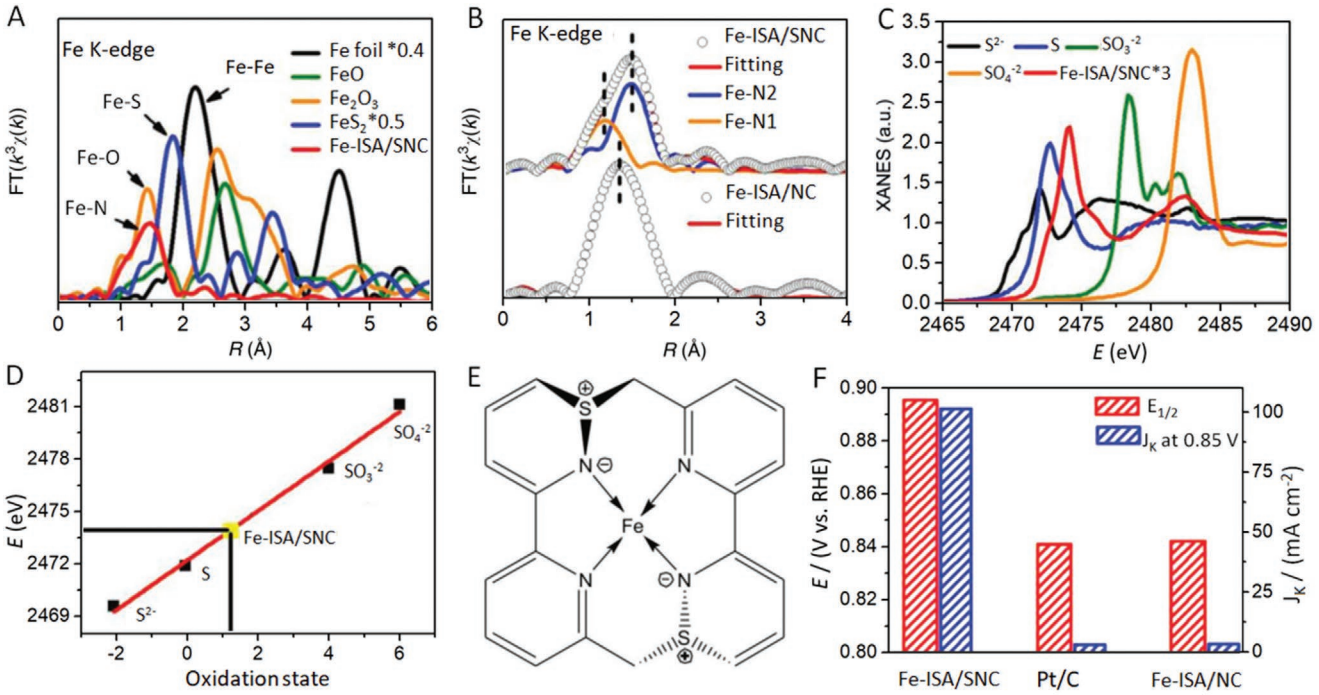

Figure 11. A) Fourier-transformed EXAFS spectra of the Fe K-edge in the S modified Fe–N_4/C catalyst and references. B) Comparison of the quantitative EXAFS fits between Fe-ISA/SNC (containing S) and Fe-ISA/NC. C) The S K-edge XANES spectra of Fe-ISA/SNC and reference materials D) with the corresponding linear fit. E) The molecular structure of the FeN_4S_2 active site in Fe-ISA/SNC. F) Kinetic current density (J_k) at 0.85 V versus RHE and $E_{1/2}$ of Fe-ISA/SNC, Fe-ISA/NC, and Pt/C. A–F) Reproduced with permission.[161] Copyright 2018, Wiley-VCH.

step of the hydrogenation of adsorbed O_2 can be improved, further enhancing the ORR activity. A similar effect has been predicted in the B-doped system, B-MN_4.[168]

The presence of a heteroatom dopant bonded to C atoms in the vicinity of the M–N_x center can also impact the performance.[164–166,169–171] Typically, these heteroatom dopants have the following catalytic roles: 1) to optimize the adsorption energies of intermediate species to speed up the key reaction steps through tuning the charge state of metal center; 2) to form highly active sites via the redistribution of charge density of C atoms induced by heteroatoms; 3) to improve the conductivity of carbon frameworks after heteroatom doping, which thus facilitates the electron transfer; and 4) to construct a porous structure with high specific surface area to allow for fully accessible active sites. Recently, Wei et al. prepared Co_1-SAECs supported by P-doped carbon nitride (Co_1/C_3N_4) for HER.[170] An accurate determination of the atomic structure of P dopants near Co–N_4 active site remains challenging. The authors demonstrated that incorporating a P dopant near the Co–N_4 active site greatly improves the conductivity of carbon nitride as supported by electrochemical impedance spectroscopy. Operando X-ray absorption fine structure (XAFS) measurement revealed that the average oxidation state of Co atom increases from +2.02 to +2.20 and +2.40 under the open-circuit condition and at the negative potential of −0.04 V versus RHE near the onset HER potential, respectively. These results indicate that the Co–N_4 active site will evolve into Co–N_2O (two-coordinated Co–N_2 with one coordinated Co–O) and Co–N_2O_2 (two-coordinated Co–N_2 with a two-coordinated Co–O_2) under these conditions, respectively. Such a dynamic change of the local bonding configuration is also captured in the Fourier-transformed EXAFS spectra of Co K-edge (**Figure 12**A,B). Moreover, operando Fourier-transform infrared spectroscopy (FTIR) analysis also reveals an increase in the intensity of OH stretching mode for Co_1/C_3N_4 under both the open-circuit condition and at the negative potential of −0.04 V versus RHE. In this process, the P dopant plays an important role in promoting electron transfer to form a highly active site (HO–Co_1–N_2) for HER, displaying comparable performance to Pt/C.

Heteroatom doping of SAECs can lead to different electrocatalytic performance, depending on the nature of the metal atom and its interaction with proximal atoms. For instance, the presence of S bonded with C near the CuN_4 center possesses a lower energy barrier toward the OOH* formation than that of the catalytic site (S bonded with N in CuN_4), which facilitates the key step of ORR. This optimized microstructure of S doped CuN_4-SAECs is dramatically distinct to S doped FeN_4-SAECs (S bonded with N in FeN_4).[161,166] The key point of heteroatom engineering for improving electrocatalytic activities lies in the appropriate modulation of electron density over MN_x sites, which can lower the activation energy barrier for critical steps in the electrocatalytic reactions.

4.2. Vacancy/Edge Structures

Engineering vacancy/edge near a single-metal center can also lead to the formation of new highly active single-metal sites because the presence of these defect structures can optimize the electronic structure of the catalytic center and increase its accessibility during electrocatalysis.[13] For instance, defective carbon materials can act as superior supports for the fabrication of high-performance SAECs, such as Ni_1-SAECs,[172] Pt_1-SAECs,[98] and Co_1Pt_1-SAECs.[28] Li et al. recently demonstrated a thermal emission strategy for the preparation of several precious meta-based (Pt, Au, and Pd) SAECs on defective graphene oxide. It is found that defects in graphene modify the local electronic structure of anchored Pt_1, thereby tuning its electrocatalytic activity. For example, four-coordinated Pt (Pt_1C_4) shows a depleted electron density compared to Pt anchored on a pristine graphene host, thus weakening the adsorption of H* over Pt sites and improving the HER activity.[98] Single-atom Pt anchored in the divacancy of defective graphene (DG) shows an excellent HER performance, outperforming both Pt

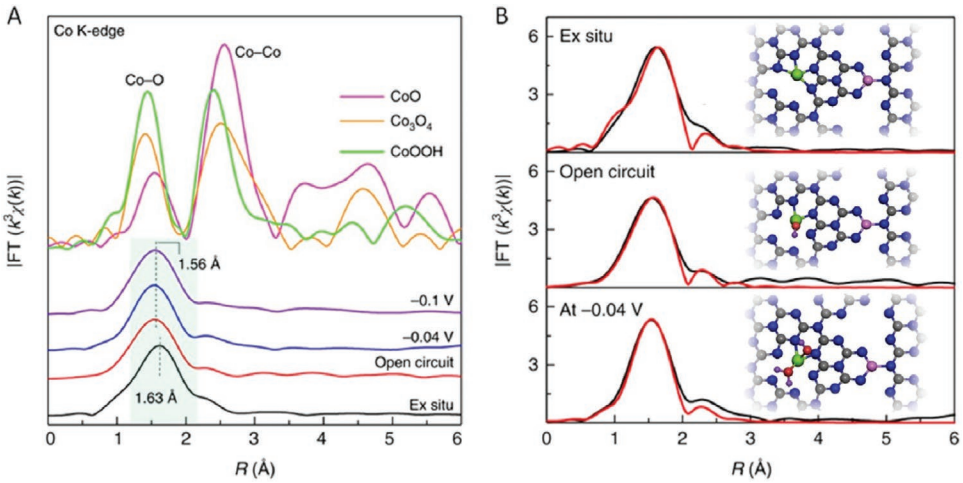

Figure 12. A) Fourier-transformed EXAFS spectra of the Co K-edge in Co_1/C_3N_4 and reference samples. B) First-shell fitting Fourier-transformed EXAFS spectra of the Co K-edge in Co_1/C_3N_4 obtained under different conditions. Insets illustrate the corresponding geometric configurations. Gray, blue, red, pink, green, and purple balls are C, N, O, P, Co, and H atoms, respectively. A,B) Reproduced with permission.[170] Copyright 2019, Nature Research.

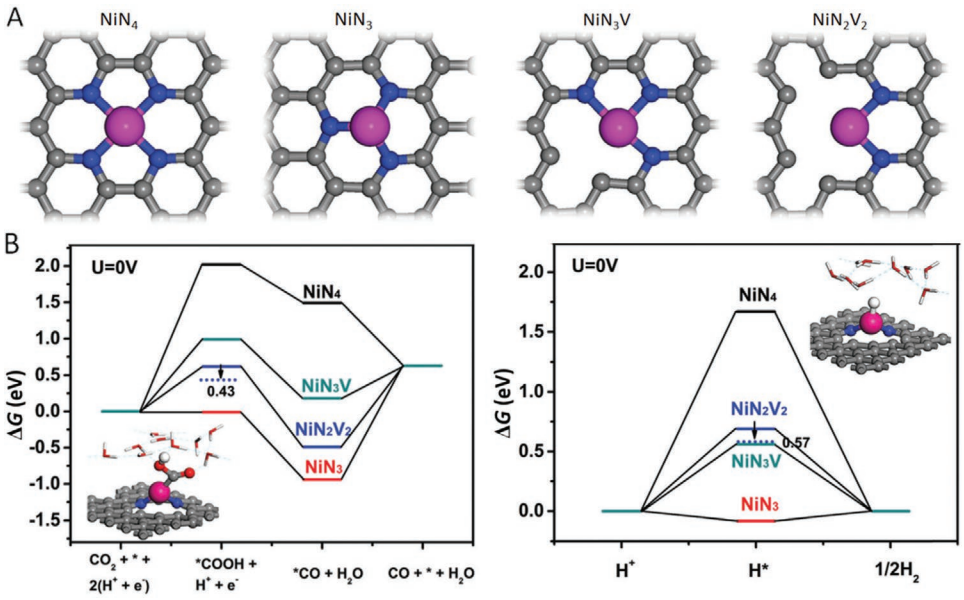

Figure 13. A) Optimized atomic structures of Ni_1-SAECs based on N-doped carbon with distinct coordination numbers and geometries. B) Free energies of CO_2RR and HER over the different Ni–Nx structures. Inset: *COOH and H* intermediates adsorbed on the NiN_2V_2 site. One water molecule layer is included to simulate the solvent environment. A,B) Reproduced with permission.[172] Copyright 2018, Royal Society of Chemistry.

nanoparticles and commercial Pt catalysts. The strong interaction between Pt and divacancy in graphene results in a more significant charge density redistribution, compared to Pt anchored on a pristine graphene host. As a result, Pt_1C_4/DG shows a more moderate ΔG_{H*} to promote the overall HER. In addition, Pt_1C_4/DG also exhibits excellent catalytic stability due to its robust Pt_1–C_4 coordination structure.

The position of defects/edges near the first coordination sphere also influences the catalytic activity of SAECs.[173–176] Ni_1-SAECs containing different coordination vacancies near the center of NiN_x present distinct selectivity for the CO_2RR into CO, which include the Ni atoms coordinated with 4 N atoms (NiN_4), 3 N atoms (NiN_3 and NiN_3V, V denotes a coordination vacancy), and 2 N atoms (NiN_2V_2) (**Figure 13**A).[172] The H* adsorption is weaker over NiN_3V and NiN_2V_2 sites compared to NiN_3, implying that NiN_3 is a superior active site for HER (Figure 13B). The NiN_3V structure with one coordination vacancy presents a lower energy barrier from *CO to CO compared to NiN_3, indicating that the presence of vacancy structure in Ni_1-SAECs has a positive effect on the reduction of CO_2 to CO product. It is also found that ΔG_{*COOH} is lower than ΔG_{H*} for NiN_2V_2 with/without considering the solvent effect, which suggests the adsorption of COOH* is stronger than that of H*. Therefore, this SAEC shows high selectivity for the CO_2RR toward CO production, partially due to the suppression of the competing HER process. NiN_2V_2 presents moderate adsorption energies of intermediates throughout the whole CO_2RR process, and thus shows excellent activity for CO_2RR into CO. In addition, the free energies of ΔG_{*COOH} over NiN_3, NiN_3V and NiN_2V_2 sites are significantly lower than those over the NiN_4 site, indicating that the high CO_2RR activity is associated with undercoordinated Ni–N sites. Based on the above analysis, vacancy structure in Ni_1-SAECs plays a dominant role in the optimization of CO_2RR performance. NiN_2V_2 with coordinatively unsaturated Ni–N sites shows high selectivity for CO production due to the suppression of HER and enhancement of *COOH formation, superior to NiN_3C (Ni coordinated with three pyridinic-N atoms and one C atom).[133]

Besides coordination vacancies, the removal of C atoms near M–N_x sites creates C vacancies that can enhance the intrinsic activity through the optimization of free energies of reaction intermediates over the catalytic centers.[173–175,177] Chen et al. prepared Fe_1-SAECs supported by a highly nanoporous carbon.[173] The introduction of an NH_4Cl agent in the thermal decomposition of polyaniline could release a large amount of gases (NH_3 and HCl), creating an abundance of nanopores with exposed carbon edges in the pyrolyzed carbon materials. Theoretical calculations reveal that C vacancy/edge near the Fe–N_4 site greatly enhances the chemical adsorption of O_2 and promotes the $4e^-$ process for ORR in a high-power density half-cell test for PEMFC. Wang et al. also studied the effect of different types of C vacancies on the ORR over Fe–N_4 species (**Figure 14**).[174] At the equilibrium potential of $U = -0.77$ V (vs standard hydrogen electrode (SHE)), the $4e^-$ reduction pathways showed a negative ΔG. However, the first electron transfer step ($*O_2 + H_2O + e^- \rightarrow *OOH + OH^-$) became the potential-limiting step with the largest positive ΔG at $U = 0.13$ V (vs SHE). Among all the atomic models tested, FeN_4-6r-c2 possessed the most appropriate ΔG for each reaction step, superior to FeN_4 sites without the presence of C vacancies. In addition, dangling bonds at carbon edges can also influence the intrinsic activity of M–N_4 sites. For example, S doping at carbon edges (C–S) near Fe–N_4 resulted in the strong adsorption of *O and *OH species, leading to lower ORR activity compared to an ideal Fe–N_4 site. In contrast, the presence of oxidized S groups (C–SO_2) at carbon edges decreased the d-band centers of iron via an electron-withdrawing effect, which lowered the adsorption energies of *O and *OH, improving the ORR activity in

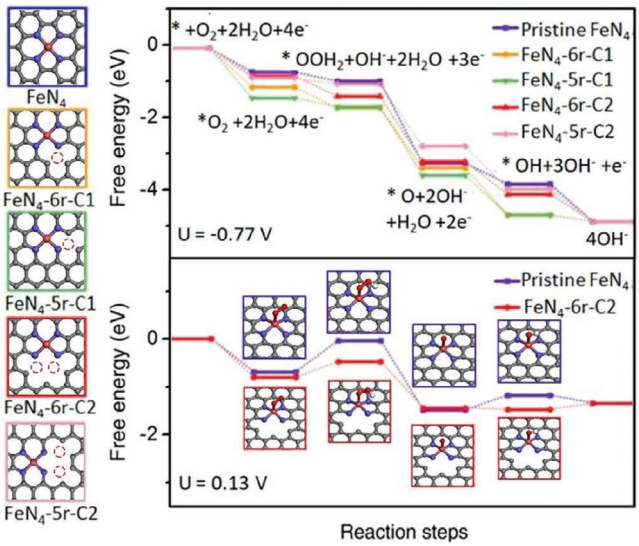

Figure 14. ORR free energy diagrams (U = –0.77, 0.13 V vs SHE) of five possible atomic configurations (6r or 5r refers to the six- or five-membered Fe–N-heterocyclic ring, respectively; c1 or c2 refers to the cleavage of one or two C—N bonds adjacent to Fe–N_4, respectively). Reproduced with permission.[174] Copyright 2018, American Chemical Society.

acidic medium.[177] This work demonstrates that the electron density of M–N_4 sites can be controlled by tuning adjacent functional groups. Moreover, the nanopores present in NPM-SAECs can facilitate the diffusion of intermediates during the reaction to accelerate the kinetics.[178] Therefore, edge-site engineering of geometric and electronic structures of SAECs provides a new pathway to improve their performance.[179–181]

4.3. Dual Sites (M1–O/N–M2)

Dual metallic SAECs consisting of two single metal sites connected via a nonmetal atom linker (e.g., M1–O/N–M2) such as Pt–O_2–Fe,[159] Zn–N–Co,[160] and Fe–O_2–Co[182] can benefit from synergistic interactions, originating superior electrocatalytic activity compared to monometallic SAECs and commercial Pt/C catalysts.[183] The local environment of a dual metallic site, including its coordination number and chemical bond, is distinct from an isolated atom of an individual metal. In addition, the electronic interactions between two metal atoms through bridging atoms (e.g., O, N) can lead to electron density redistribution, which may change the charge state of the metal.

Pt nanoparticles and its alloys are considered as the best ORR catalysts for the $4e^-$ catalytic processes, while Pt_1-SAECs have been proved to be highly efficient ORR catalysts for $2e^-$ catalytic processes.[94,184–186] Such different electrocatalytic behavior between Pt_1-SAECs and Pt nanoparticles is largely attributed to the different chemical structures of Pt atoms. Interestingly, dual-metal active sites containing Pt and another metal atom shows an excellent ORR performance for $4e^-$ catalytic processes. This suggests that the electronic properties of Pt in dual-metal SAECs can differ significantly from an isolated single Pt atom in Pt_1-SAECs. As shown in **Figure 15**A–C, Pt atoms can be grafted to the Fe atom of Fe–N_4 centers via two bridging oxygen atoms (Pt_1@Fe–N–C), creating a new active moiety of Pt_1–O_2–Fe_1–N_4 in carbon support for tri-catalytic systems including ORR, OER, and HER.[159] A single Pt atom anchored on Fe–N_4 site efficiently suppresses the production of H_2O_2 during ORR. Therefore, H_2O_2-induced electrooxidation of carbon materials can be avoided, which improves ORR stability. Pt_1@Fe–N–C exhibits a modest ΔG_{H*} closer to zero compared to both Fe–N–C and Pt_1@C, resulting in excellent HER performance.

In another example, Yao et al. successfully prepared atomically dispersed Co and Pt atoms embedded in the N-doped carbon support (Co–Pt/N/C) through a combination of thermal pyrolysis and electrochemical deposition.[28] Single Co and Pt atoms are embedded in N doped carbon to form a bimetallic center consisting of two adjacent CoN_4 and PtN_4 sites (Figure 15D). In contrast to the aforementioned Pt_1-SAECs with low activity and selectivity for ORR (favoring the production of H_2O_2 rather than H_2O), bimetallic Co–Pt/N/C exhibits an excellent ORR activity with an outstanding half-wave potential of 0.96 V versus RHE, much higher than that of Pt/C (0.87 V vs RHE). Such a high activity is expected to originate from the synergistic effect between atomic Co and Pt atoms anchored at a N-doped carbon vacancy site. DFT calculations reveal that the Co 3d orbitals of Co–Pt/N/C are energetically closer to E_F than Pt 5d orbitals of Pt–Pt/N/C, indicating a strong binding between O and Co–Pt/N/C. Additionally, a polarization of surface charge near the dual-metal sites results in a strong electron accumulation around the Co atom and a weak electron accumulation or depletion around Pt (Figure 15E). This is attributed to the asymmetric deployment of Pt and Co that polarizes the surface charge near the Co–Pt center. An accumulation of electron density over the Co site would accelerate the reduction of O_2 and thus enhance the ORR performance. Besides, reaction intermediates show different adsorption behaviors over dual site SAECs. For example, a dual Co and Zn center linked by N atoms exhibits a higher activity for O_2 activation than monometallic Co and Zn centers (Figure 15F,G), reducing the dissociation barrier of O_2. The O—O bond length can be elongated from 1.23 to 1.35 Å over the Zn–N–Co center, much longer than that over Co (1.28 Å) and Zn (1.31 Å), respectively.[160] Similarly, the incorporation of dual metal sites for the regulation of their overall catalytic activity is also demonstrated in other bimetallic SAECs, including Fe–O_2–Co, Pt–N–Ru, and Fe–N–C–N–Co.[182,187,188]

5. Activation of the Host by Single Atom Doping

Single metal atoms anchored on a support not only constitute highly active site for electrocatalytic reactions, but can also tune the electronic structures of host materials. The latter effect based on single atom dopants can generate new phases in the host and activate atomic sites in the support for electrocatalysis.[92,99,189] To date, numerous metal chalcogenides-based SAECs are designed based on these two factors, which can further optimize the adsorption energies of intermediate species to speed up the key reaction steps in certain electrochemical conversions. In this section, we will highlight the recent efforts on the regulation of local electronic structures of various SAECs by

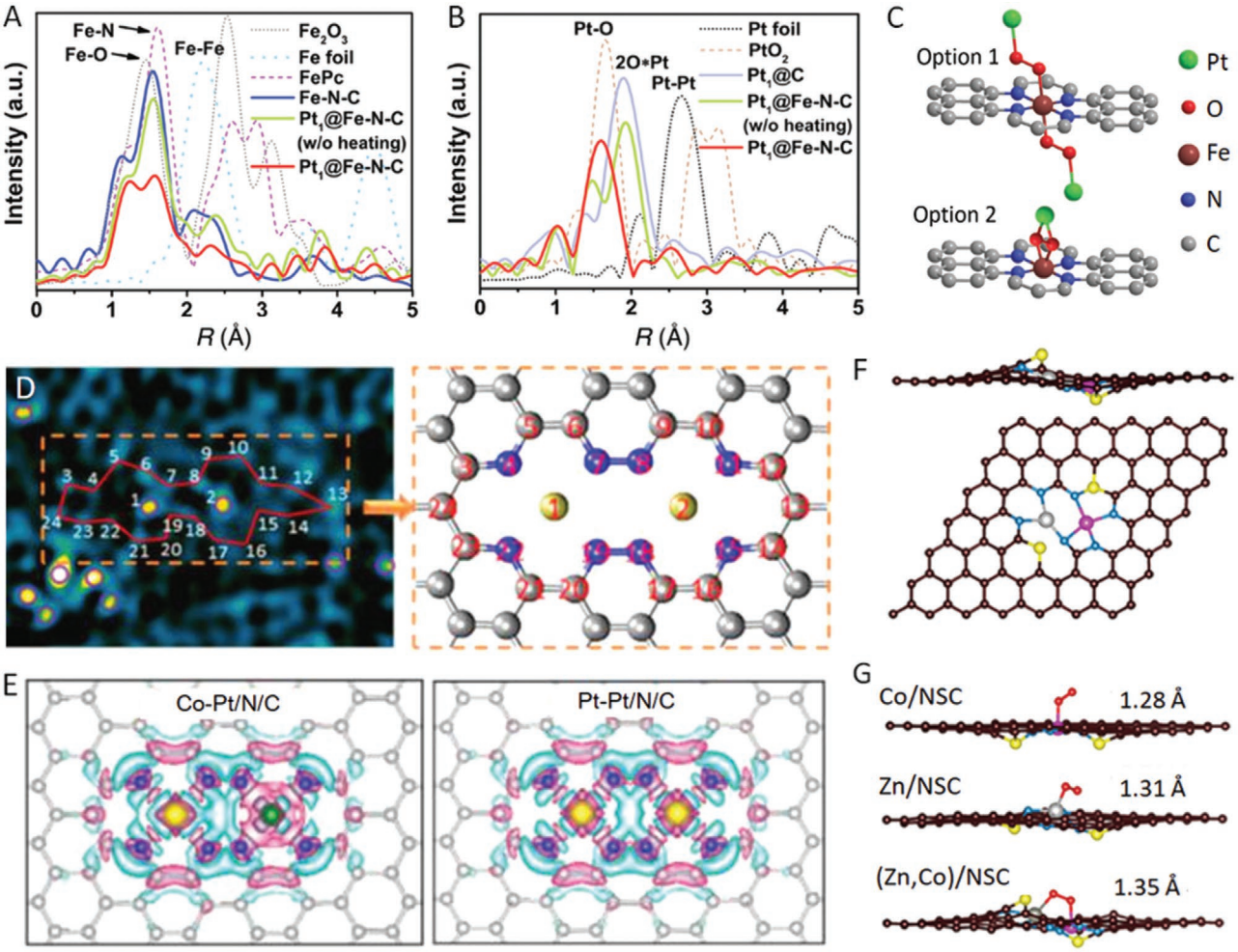

Figure 15. A) FT k^3-weighted Fourier-transformed EXAFS spectra of Fe K-edge in Pt_1@Fe–N–C, Pt_1@Fe–N–C (w/o heating) and references. B) FT k^3-weighted Fourier-transformed EXAFS spectra of Pt L_3-edge in Pt_1@Fe–N–C, Pt_1@Fe–N–C (w/o heating) and references. C) The proposed structure of the active site of Pt_1@Fe–N–C. D) HAADF-STEM image of Co–Pt/N/C after fast Fourier transformation filtering (left) with the proposed structural model of the two metal atoms trapped in the defect-containing C/N graphene (right). Metal, carbon and nitrogen atoms are colored yellow, gray, and blue, respectively. E) Top view of the charge densities of the Co–Pt/N/C and Pt–Pt/N/C catalysts. Pink and aqua isosurfaces represent electron accumulation and depletion areas with an isosurface level of 0.0025 e/a_0^3, respectively. F) Optimized geometry of the (Zn,Co)/nitrogen and sulfur codoped carbon (NSC) in the calculations. G) Optimized geometries of O_2 adsorption configuration on the Co/NSC, Zn/NSC, and (Zn,Co)/NSC. Brown, blue, yellow, red, gray, and pink balls are C, N, S, O, Zn, and Co atoms, respectively. A–C) Reproduced with permission.[159] Copyright 2018, Wiley-VCH. D,E) Reproduced with permission.[28] Copyright 2018, American Chemical Society. F,G) Reproduced with permission.[160] Copyright 2019, Elsevier.

tuning the catalytic properties of atomic sites in the host via a single atom dopant (**Figure 16**).

5.1. Nearest Neighbor Activation

Nanostructured metal chalcogenides show highly intrinsic activities for both HER and OER, especially for transition metal dichalcogenides (TMDs, MX_2, M = Mo, W or V, and X = S or Se),[190,191] which have been actively explored in renewable energy conversions. Their electrocatalytic performance closely relates to the electronic structures of the exposed active sites, which can be further tuned by multiple approaches such as phase engineering, defect engineering, interlayer engineering, and heteroatom doping. Among all these methods, heteroatom doping is considered as an efficient approach for tuning the electronic properties of metal dichalcogenides. The majority of heteroatoms including metals and nonmetals in MX_2 possess two possible configurations, involving the substitution of M or X atoms, respectively. These two configurations can activate the host's atomic site toward an enhanced electrocatalytic performance.

The substitution of M in TMDs via other metal species has been demonstrated for Pt,[192] Au,[193] V,[194] Co,[195] Mn,[196] Ni.[197,198] The heteroatom substitution of M modifies the electronic structures of the nearest X atom in TMDs, which can be activated as a new catalytic center. For instance, the DOS around E_F (mPF-MoS_2) of in-plane S sites for mesoporous MoS_2 foam can be significantly increased after doping with atomically dispersed Co atoms (**Figure 17**A).[195] When a H atom is absorbed over a S atom in doped MoS_2, the hybridization of the H 1s orbital and the S 3p orbital leads to the formation of a bonding orbital (δ) and antibonding orbital (δ^*) according to

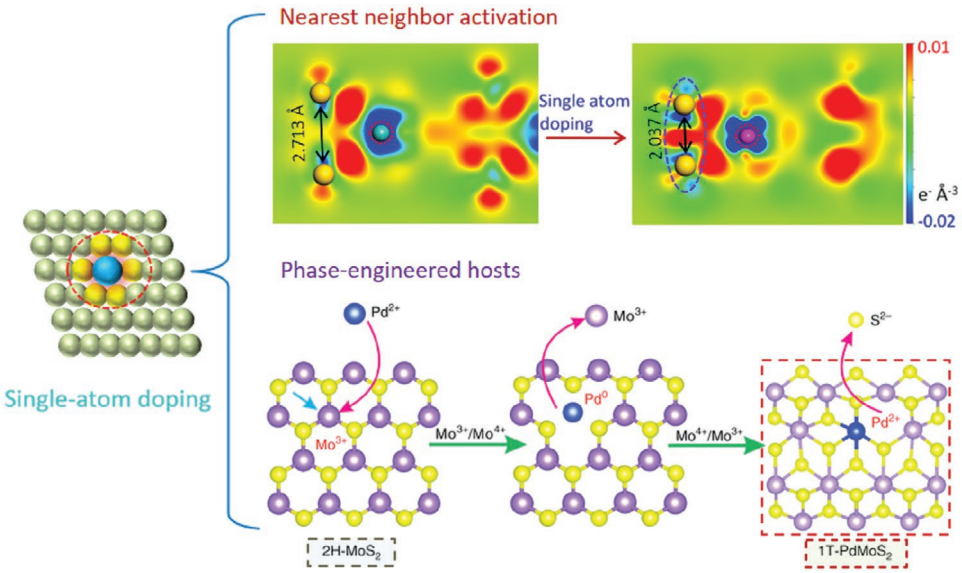

Figure 16. Single-atom doping for the enhancement of the electrocatalytic performance. i) Activation of the nearest atomic sites in the host by introducing a single-atom dopant. ii) Phase engineering of the host materials. Reproduced with permission.[203] Copyright 2019, Nature Research.

molecular orbital theory. The S 3p orbital is energetically well above the H 1s orbital. This gives rise to a weak H adsorption on the basal plane of pristine MoS_2 (ΔG_{H^*} = 2 eV), which detriments the HER performance of the host. When Co atoms are doped into the basal plane of MoS_2 (mPF-Co-MoS_2) after forming Co—S bonds, the electron density of the S atoms will be reduced to offset the mismatch of the energy level between the H 1s and the S 3p orbitals, hence enhancing H adsorption (Figure 17B). However, a further increase of the Co dopant density (>16.7 wt%) caused a drastic reduction in the electron density of S atoms, resulting in lower HER activity due to a strong interaction between the H and S atoms (Figure 17C). In addition, a single metal dopant in MX_2 can efficiently modulate the band gap of the host. For example, Pt atoms anchored in MoS_2 via the formation of Pt—S bonds, prepared by a one-pot solvothermal method, successfully triggers the HER activity of in-plane S atoms neighboring the doped Pt atoms (Figure 17D,E).[192] DFT calculations reveal that the Pt-doping of MoS_2 results in a downward shift of the valence band and an increased number of hybridized electronic states near E_F, which thus improves the conductivity of MoS_2. Moreover, the electronic states of in-plane S sites adjacent to the Pt dopant around E_F increase significantly, leading to enhanced H adsorption over the in-plane S atoms of Pt–MoS_2, which is beneficial for the HER. In general, an enhancement of the HER activity of the chalcogen atomic site near single-metal dopants in TMDs can be linked to an increased abundance of unsaturated S atoms surrounding the heterodopant.

Besides metal doping, the substitutional replacement of chalcogen atoms in TMDs by nonmetal heteroatom dopants, including C,[199] N,[200,201] and P,[202] can effectively modify the electronic and catalytic properties of TMDs. C doped MoS_2 synthesized via controlled sulfurization of Mo_2C shows an excellent HER performance comparable to commercial Pt catalyst in alkaline medium.[199] The C dopants tend to undergo sp^2 hybridization leaving an unhybridized $2p_z$ orbital perpendicular to the basal plane of TMDs. Such a unique orientation of the $2p_z$ orbital favors the head-on orbital overlapping for the formation of sigma bonds, which can act as active sites for water adsorption and activation. The electron density of the nearest S atoms to the C—Mo bond is reduced, which thus attracts H_2O molecule and facilitate its dissociation due to the generated empty orbitals of 2p from C doping. Charge analysis also shows that C–MoS_2 presents a strong chemical interaction between H_2O and C–MoS_2 as opposed to the intrinsic MoS_2. Therefore, C doping of MoS_2 has a similar catalytic effect to that of S, B, and P heteroatom doping of carbon-supported SAECs (Section 4.1). In addition, C-doping of MoS_2 also increases its electrical conductivity, enabling charge transfer for enhanced catalytic activity. In general, the electron density of the nearest chalcogen (X) at the nonmetal—M bond in doped TMDs can be tuned and reactivated via anion doping, giving rise toward remarkable electrocatalytic performance.[200–202]

5.2. Phase-Engineered Hosts

It has also been demonstrated that single-atom doping strategy can be used for the phase-engineering of TMDs to improve the electron transfer during the electrocatalytic processes. Typically, a phase transformation from semiconducting 2H (trigonal prismatic) phase to 1T (metallic) upon single-atom doping leads to a promotional effect. Recently, Xing et al. discovered that the substitution of a Mo atom by a single Pd dopant in MoS_2 not only introduces sulfur vacancies but also converts the 2H phase into a stabilized 1T structure (**Figure 18**A).[203] Defective 2H-MoS_2 with a stoichiometry of 1:1.87 (Mo:S) contains a portion of Mo(III) species. Therefore, the defective MoS_2 can react with Pd^{2+} to form Pd—S bond in MoS_2 via a redox coupled reaction [Mo(III)/Mo(IV) and Pd(0)/Pd(II)], resulting in a phase transformation from 2H into the stabilized 1T phase as demonstrated by Raman spectroscopy (Figure 18B,C). The 1T

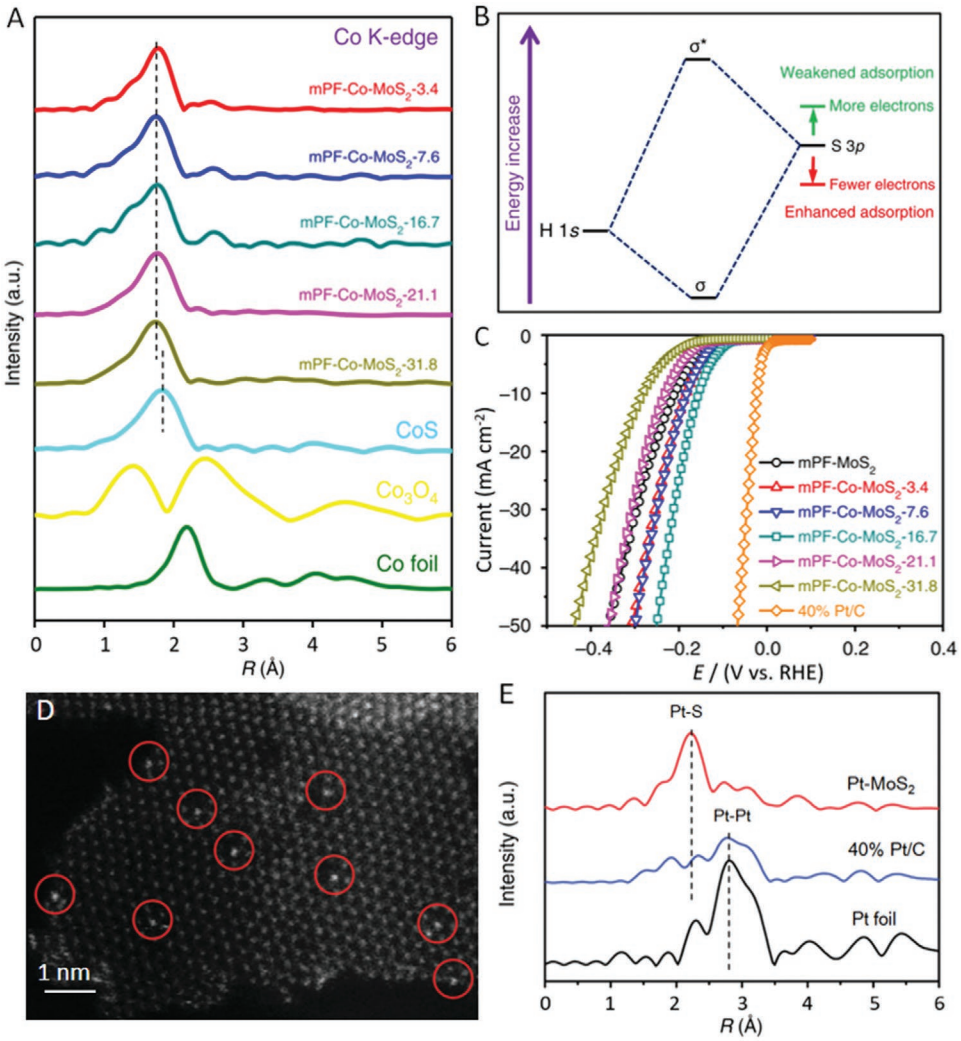

Figure 17. A) Co K-edge k_2-weighted EXAFS spectra of a series of mPF-Co-MoS_2 samples and some references. B) Schematic diagram illustrates the bonding of H 1s orbital and S 3p orbital (from MoS_2). The depletion of electrons on S atoms lowers the orbital position and strengthens the H—S bond. C) HER polarization curves for mPF-Co-MoS_2 with different Co doping contents in comparison with mPF-MoS_2 and 40% Pt/C. D) HAADF-STEM image of Pt–MoS_2. Single Pt atoms are marked by red circles. E) Fourier transforms of k^2-weighted Pt EXAFS for Pt–MoS_2 in comparison to Pt foil and commercial 40% Pt/C. A–C) Reproduced with permission.[195] Copyright 2017, Nature Research. D,E) Reproduced with permission.[192] Copyright 2015, Royal Society of Chemistry.

phase is metallic and facilitates electron transfer during the HER process. The single Pd dopant also effectively activates the neighboring S sites for the HER. A similar effect has been observed in Mn-doped MoS_2.[196] Electron donation from the Mn to Mo 4d orbitals results in an increased metallic character of MoS_2. Moreover, the doping of Mn into the lattice of MoS_2 also creates a local strain that can lead to a plane sliding of S layers, resulting in a 2H-to-1T phase transition accompanied by the creation of a large number of S vacancies, as revealed by aberration-corrected scanning transmission electron microscopy (STEM) (Figure 18D,E). Therefore, hetero-metal doping of TMDs offers an efficient strategy to enhance the electrocatalytic performance through as-generated chalcogen vacancy and doping-induced phase transformation.[204,205]

Apart from metals, the crystalline phase of TMDs can also be modified by doping with nonmetal atoms. For example, 2H to 1T′-(distorted 1T) phase conversion of MoS_2 nanostructures can be achieved by N doping.[206] N-doped 1T′-phase MoS_2 exhibits a higher HER activity than pure MoS_2. An enhancement of HER activity of N-doped 1T′-phase MoS_2 is attributed to the formation of S vacancies together an increase of the DOS around E_F. Therefore, doping of TMDs with both metal and nonmetal species can act as an efficient approach to optimize the electrocatalytic activity of TMDs by phase engineering.

6. Approaches to Control the Local Structure in SAECs

Single-atom electrocatalysts supported on either carbon-based metal-free materials or metal chalcogenides have attracted considerable attention in recent years due to their great potential for a wide range of electrochemical conversions, including

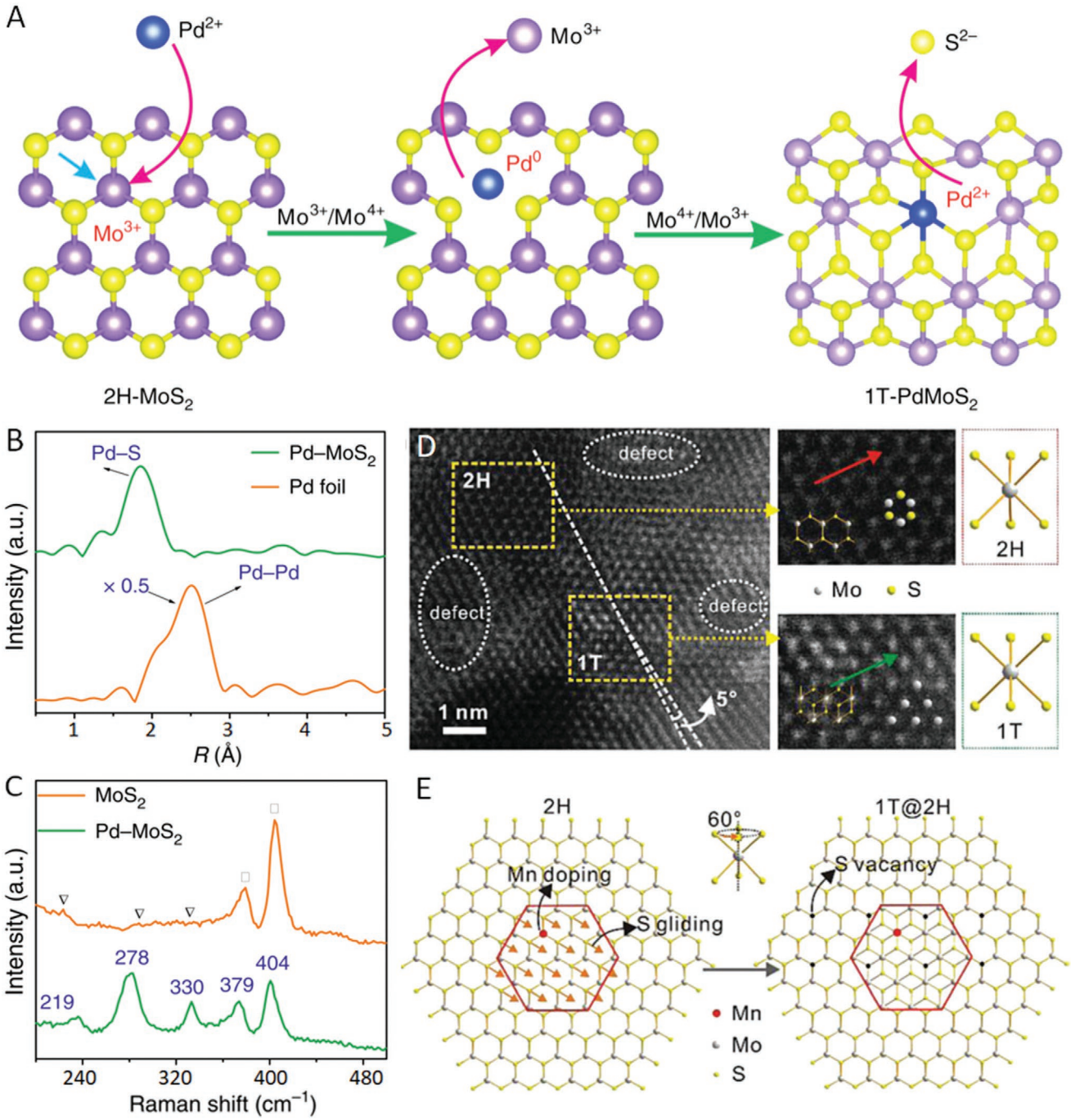

Figure 18. A) Schematic illustration of the spontaneous MoS_2/Pd(II) redox reaction. B) Raman spectra of 1%Pd–MoS_2 and MoS_2. 378 and 404 cm^{-1} are attributed to the 2H phase vibrational configuration of MoS_2; 219, 278, and 330 cm^{-1} are attributed to the 1T phase vibrational configuration of MoS_2. C) Fourier transforms of the k^3-weighted Pd K-edge of the EXAFS spectra of Pd-MoS_2 in comparison to Pd foil. D) HAADF-STEM image of a single Mn doped MoS_2 nanosheet. The 2H and 1T phases are visualized with two ball-stick models in dotted rectangular boxes; defects are visualized with dotted circles. E) A possible mechanism of phase transformation from 2H to 1T after Mn-mediation for MoS_2. A–C) Reproduced with permission.[203] Copyright 2018, Nature Research. D,E) Reproduced with permission.[196] Copyright 2018, Royal Society of Chemistry.

ORR, OER, HER, NRR, CO_2RR, FAO, etc. On one hand, the local environment surrounding a single metal site plays a key role in the modulation of the performance of these SAECs, including the activity, selectivity and stability. On the second hand, host atoms proximal to the single metal atom can be activated due to strong electronic hybridization with the doped single-metal atom. To date, numerous SAECs with unique local structures have been synthesized as efficient electrocatalysts in various energy conversions, as shown in **Table 3**. Generally, advanced single-atom electrocatalysts with tunable local

Table 3. Current methods for the regulation of various local structures of single-atom electrocatalysts.

Catalysts	Active site	Precursors	Methods	Reaction	Ref.
Fe_1/N doped graphene	Fe–N_5	Hemin, melamine, graphene	Tuning pyrolysis precursors	CO_2RR	[112]
Fe_1/N doped carbon	Fe–N_3	2-Methylimidazole, iron(II) acetate tetrahydrate, $Zn(NO_3)_2{\cdot}6H_2O$	Tuning pyrolysis precursors	NRR	[120]
Cu_1/N doped graphene	Cu–N_2	Dicyandiamide ($C_2H_4N_4$), copper phthalocyanine (CuPc)	Tuning the contents of metal precursor	ORR	[121]
Pt_1/Au nanoparticles	Single Pt	$H_2PtCl_6{\cdot}6H_2O$, $HAuCl_4{\cdot}3H_2O$	Tuning the ratio of metal precursors	FAO	[125]
W_1/N doped graphene	W–N_5	Dopamine, $Na_2WO_4{\cdot}2H_2O$, 2-amino-2-hydroxymethyl-propane-1,3-dio	Tuning the pyrolysis conditions (temperature, carrier gas and time)	ORR	[207]
Fe_1/N doped carbon	Fe–N_4 (pyrrolic N)	Aniline, $FeCl_3{\cdot}6H_2O$	Tuning carrier gas in pyrolysis	ORR	[208]
Pt_1/graphdiyne	Pt–Cl_2C_2	Graphdiyne, K_2PtCl_4	Tuning heating temperature	HER	[104]
Ru_1/N doped graphene	Ru–C_2N_2	Melamine, $RuCl_3$	Tuning heating temperature	HER	[130]
Co_1/N doped porous carbon	Co–C_2N_2	2-Methylimidazole, $Co(NO_3)_2{\cdot}6H_2O$	Tuning heating temperature	ORR	[131]
Co_1/N doped carbon	Co–C_3N	Aniline, $Co(NO_3)_2{\cdot}6H_2O$	Tuning heating temperature	HER	[132]
Sn_1/N doped graphene	Sn–C_2N_2	Graphene oxide, $SnCl_2{\cdot}2H_2O$	Tuning metal precursors and carrier gas in pyrolysis process	CO_2RR	[134]
Co_1/B, N codoped porous carbon	Co–BN_3	Polyethylene glycol, Urea, H_3BO_3, $Co(NO_3)_2{\cdot}6H_2O$	Tuning pyrolysis precursors	ORR, OER	[140]
Cu_1/S, N codoped carbon nanotubes	Cu–SN_3	Carbon nanotubes, 4,4′-sulfonyldiphenol Hexachlorocyclophosphazene $CuCl_2$	Tuning pyrolysis precursors	ORR	[142]
Co_1/N doped carbon	$CoCN_3$	2-Methylimidazole, $Co(NO_3)_2{\cdot}6H_2O$, $Zn(NO_3)_2{\cdot}6H_2O$	Tuning heating temperature	ORR	[209]
Ru_1/N doped graphene	Ru–N_4O	Graphene oxide, $Ru(NH_3)_6Cl_3$	Tuning carrier gas in pyrolysis	ORR	[146]
Fe_1/S, N codoped porous carbon	Fe–N_4Cl	5,10,15,20-Tetra(4-(imidazol-1-yl)phenyl)porphyrindine, Iron(II) acetate tetrahydrate, NaCl, KCl	Tuning pyrolysis precursors	ORR	[147]
Mn_1/N doped graphene	Mn–N_4Cl	$MnCl_2$, ethylenediamine	Tuning pyrolysis precursors	CO_2RR	[149]
Co_1Fe_1/N doped carbon	CoFe–N_6	2-Methylimidazole, $FeCl_3{\cdot}6H_2O$, $Co(NO_3)_2{\cdot}6H_2O$	Tuning metal precursors	ORR	[151]
Co_1Zn_1/N doped carbon	CoZn–N_6	Chitosan, $ZnCl_2$, $Co(CH_3COO)_2{\cdot}4H_2O$	Tuning metal precursors	ORR	[155]
Co_1Ni_1/N doped porous carbon	CoNi–N_6	Dopamine, potassium hexacyanocobaltate, $Ni(NO_3)_2{\cdot}6H_2O$	Tuning metal precursors	ORR, OER	[156]
Fe_1/S, N codoped porous carbon	Fe–N_4–S_2	Pyrrole, thiophene, iron(III) 2,4-pentanedionate	Tuning pyrolysis precursors	ORR	[161]
Cu_1/S, N codoped graphene	Cu–N_4–S_2	Dicyandiamide, CuPc, S powder, $Na_2S{\cdot}9H_2O$	Tuning pyrolysis precursors	ORR	[166]
Co_1/P doped C_3N_4	Co–ON_2–C–P	Urea, $NaH_2PO_2{\cdot}H_2O$, $Co(NO_3)_2{\cdot}6H_2O$	Tuning pyrolysis precursors	HER	[170]
Ni_1/N doped porous carbon	Ni–N_2 with coordination vacancies	2-Methyl imidazole, $Ni(NO_3)_2{\cdot}6H_2O$	Tuning heating temperature	CO_2RR	[172]
Fe_1/N doped carbon	Fe–N_4 with C—N bond cleavage	2-Methylimidazole, FePc	Tuning the contents of metal precursors	ORR	[174]
Co_1Pt_1/N doped carbon	Co–N_4–Pt–N_4	4,4′-Bipyridine, $Co(NO_3)_2{\cdot}6H_2O$, Pt wire	Tuning metal precursors	ORR	[28]
Fe_1Pt_1/N doped carbon	Fe–N_4–O_2–Pt	2-Methylimidazole, iron acetate, 1,10-phenanthroline, $H_2PtCl_6{\cdot}6H_2O$	Tuning metal precursors	ORR, OER, HER	[159]
Co_1Zn_1/S, N codoped carbon	Co–N_3–Zn–N_3–S_2	Urea, sodium diethyldithiocarbamate trihydrate, cobalt acetate, $ZnCl_2$	Tuning metal precursors	ORR	[160]
Co_1Fe_1/N doped carbon	Co–NCO_2–Fe	1,10-Phenanthroline, $Co(CH_3COO)_2{\cdot}4H_2O$, $Fe(NO_3)_3{\cdot}9H_2O$	Tuning metal precursors	OER	[183]
Pt_1/MoS_2	In-plane S sites	$(NH_4)_6Mo_7O_{24}{\cdot}4H_2O$, $H_2PtCl_6{\cdot}6H_2O$	Tuning metal precursors	HER	[192]
V_1/NiS_2	Ni sites	$NiCl_2{\cdot}6H_2O$, VCl_3, H_2S	Tuning metal precursors	HER, OER	[194]
Co_1/MoS_2	In-plane S sites	$(NH_4)_6Mo_7O_{24}{\cdot}4H_2O$, $Co(NO_3)_2{\cdot}6H_2O$	Tuning the contents of metal precursor	HER	[195]
C_1/MoS_2	In-plane S sites	Mo_2C, S powder	Tuning heating temperature	HER	[199]
Pd_1/MoS_2	In-plane S sites	Thiourea, palladium acetate, $(NH_4)_6Mo_7O_{24}{\cdot}4H_2O$	Tuning metal precursors	HER	[206]
Co_1/MoS_2	In-plane S sites	Thiourea, $(NH_4)_6Mo_7O_{24}{\cdot}4H_2O$, $Co(NO_3)_2{\cdot}6H_2O$	Tuning the contents of metal precursor	HER, OER	[210]

structures can be fabricated using both wet- or dry-chemical methods via i) tuning the concentration and type of metal species; ii) controlling the content and type of precursors used for the preparation of SAECs; iii) optimizing the heat-treatment conditions (temperature, time and carrier gas). However, the fundamental knowledge for precisely tuning the local structures of SAECs remains elusive at this stage. Therefore, we will provide a brief discussion on the current approaches to control the local structures of SAECs as follow.

It has been reported that the coordination number of single metal atom can be tuned by optimizing the types/contents of precursors. A judicious choice of the appropriate metal-containing precursors with predesigned coordination environment has been widely used to modulate the electronic and catalytic properties of synthesized SAECs, to achieve the desired coordination numbers or types of proximal atoms.[146,147] Tuning the chemical identity of proximal atoms (e.g., C/N, S/N) of carbon-based SAECs can be achieved by controlling the pyrolysis temperature, due to the variations in formation energies of different coordination configurations for single-metal atoms.[123,128] The pyrolysis method involving the usage of NH_3 as the carrier gas or precursor often results in releasing a large amount of gases (such as NH_3, HCl, CO, and CO_2) during thermal heating, which can create coordination vacancies and exposed edges near the first coordination sphere of metal centers for modulating the catalytic activity of single-metal site.[173,180] The presence of single metal centers is predicted to lower the formation energy of coordination vacancies and exposed edges near the metal centers.[174] In addition, the co-existence of coordination vacancies and exposed edges also provides more sites to anchor single metal atoms, and thus optimize their electronic properties and stability for superior electrocatalytic performance.[28,98,172] Dual single-metal centers can be constructed by either of these methods i) using precursors containing two kinds of metals, or ii) two-step synthesis consisting of first, a pyrolysis process and second, an electrochemical deposition.[28,183]

For the SAECs supported by metallic substrate or metal chalcogenides, the choice of metal precursors is crucial for tuning the coordination number of single-metal atom, or the nature of adjacent metal species of the host chalcogenide atoms with highly catalytic activity.[192,194,199,204] The key to modulating the catalytic properties of doped single- metal atom/host atom prepared through different approaches lies in the regulation of its charge density via forming different chemical bonds of metal with proximal atoms. This can be used to optimize the adsorption energies of the intermediate species, speeding up key reaction steps in certain electrochemical conversions.

Despite rapid progress, it still remains a great challenge to develop reliable approaches for the construction of stable SAECs with optimized metal loadings for practical applications. Generally, SAECs with high metal-loading can provide sufficient actives sites to accelerate the reactions. However, some SAECs with low metal-loading (<2.5 wt%) are reported to perform better than those SAECs with high-loading content (>8.5 wt%).[115,116,172–174,211,212] First, an increased metal loading has a strong impact on the electronic structures of the single-atom decorated support.[195] Secondly, a large number of single-atom sites in high-loading SAECs may be embedded in the bulk and inaccessible to the reactants. Therefore, the interplay of these factors results in an optimal metal loading of SAECs.

Currently, the majority of SAECs are prepared via chemical treatment under harsh condition (e.g., acidic washing for the removal of metal nanoparticles). The strong bonding of single atoms with the support ensures the atomic dispersion of single atoms and prevents their leaching even under operating conditions. Unfortunately, the activity of SAECs often decreases in the long-term electrocatalytic testing, due to the instability of catalytic supports.[8,16] For example, the degradation of catalytic supports becomes a major issue in carbon-based SAECs for electrocatalysis,[16,213,214] especially for the ORR and OER. In addition, some species in the support of metal-based SAECs react with intermediates, resulting in the damage of atomic environments of SAECs.[13,99] Therefore, searching robust support to strongly anchor single-atoms is crucial to construct excellent SAECs with high stability under operation conditions.[92,93,215]

7. Summary and Perspective

The performance of SAECs closely relates to the local structure of the active metal and its electronic interaction with the host. The chemical hybridisation of atomically-dispersed single atoms with the support gives rise to unique electronic properties compared to metallic nanoparticles and bulk materials, leading to superior reactivity and selectivity of SAECs in renewable energy conversions. The chemical environment of metal atoms on the support is defined by several parameters, including the coordination number, chemical identity of proximal atoms, the nature of first and second nearest neighboring atoms to the single metal atom. Supported metal atoms are usually under coordinated compared to their nanoparticle counterparts. The electronic hybridization leads to charge density redistribution between the isolated metal and adjacent atoms in the host, which offers a promising way to tune the valence state and thus regulates the chemical interaction strength (adsorption energies) with reactants or intermediate species. In addition, the electronic structures of host materials can be modified by the single-atom dopants. Such an effect could trigger the intrinsic activity of host atoms neighboring the doped metal. Simultaneously, local defects including heteroatoms/vacancy/edge surrounding single-atom active sites can be used to engineer the electronic properties of a supported single-metal atom, whereby the adsorption energies of reactants/intermediates over catalytic sites can be optimized.

Engineering the local structure of supported single atoms toward increased near-Fermi electronic states often leads to the formation of highly active sites, with a dramatic decrease of the energy barriers of the potential-limiting steps associated with the electrochemical conversions. On the other hand, hetero-metal atom doping can be utilized to induce the semiconductor-to-metal phase transition in the host, which can improve the conductivity of the substrate and thus facilitate electron transfer in the electrocatalysis. In addition to monometallic SAECs, dual-metal centers can exhibit a superior catalytic performance due to synergistic interactions, unmatched by

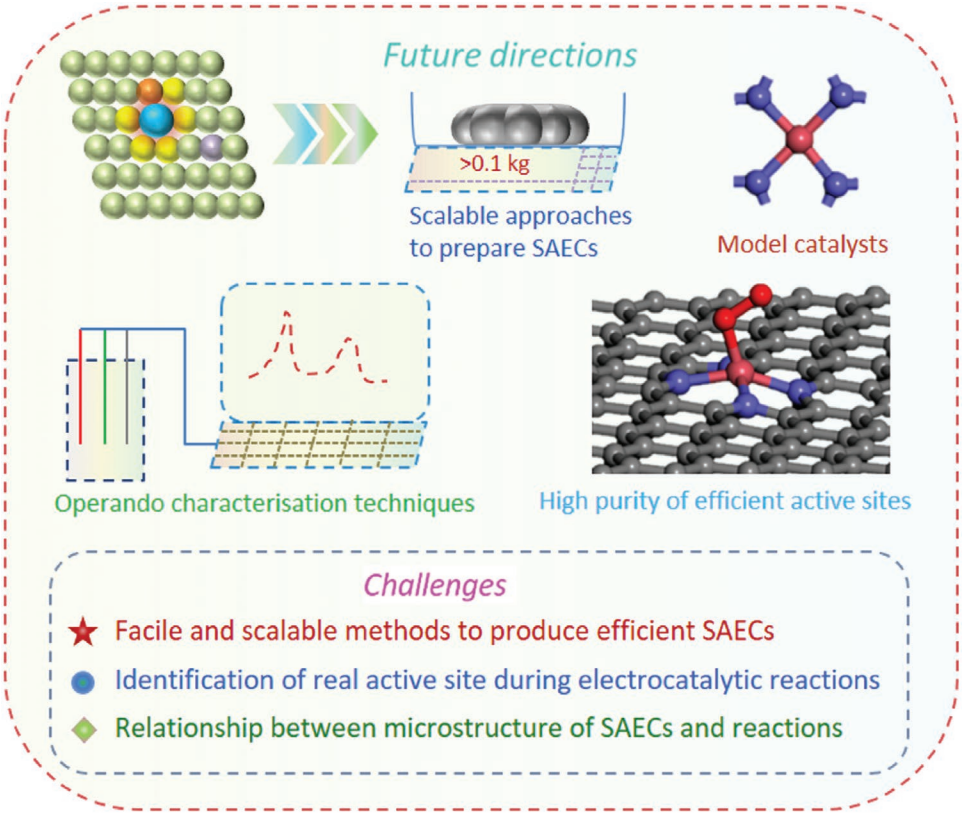

Figure 19. Major challenges and future directions in the design of advanced SAECs for electrochemical conversion.

a single metal. As-optimized local structures of SAECs often differ for different electrocatalytic reactions, such as CoC_2N_2 for ORR, CoC_3N for HER, WN_5 for ORR, WC_3N for HER, FeN_5 for CO_2RR, and FeN_3 for NRR. The desired local structure of single-metal centers also varies for different metal species even for the same electrochemical reactions. Because of this, there are plenty of possibilities in the rational construction of highly active SAECs by engineering the local structure of the single-metal center, i.e., the first and second coordination spheres and beyond, and by single-atom doping. Despite rapid progress in the field, several major challenges still need to be overcome for the design and synthesis of advanced SAECs to enable their widespread practical application (**Figure 19**). Here, we highlight current critical issues and possible future directions in the field of SAECs:

1. The availability of facile and scalable approaches is a prerequisite for the implementation of high-performance SAECs with precisely tailored chemical environments for renewable energy conversions. The ultimate goal is to replace the current precious-metal-based electrocatalysts with more abundant transition metals. Despite the very promising performance, SAECs have not been widely adopted in industrial applications, presumably due to the following unsolved issues. First, the costly precursors and multiple-steps involved in most synthetic approaches (e.g., chemical synthesis of exotic precursors, thermal pyrolysis and extensive acidic washing) are not amenable to large-scale production at low cost. Second, their electrocatalytic performance in terms of efficiency and stability are not comparable to those of precious metal-based SAECs or benchmark commercial catalysts, especially for fuel oxidation reactions (e.g., FAO), ORR for H_2O_2 production, as well as CO_2RR to C_n ($n \geq 2$) hydrocarbons.
2. Precise identification of the atomic structures of single-atom active sites is also recognized as an important challenge because it is crucial to establish accurate relationships between the local architecture and performance of SAECs. Currently, STEM has been intensively used to image the spatial distribution of atomically dispersed metal sites. However, it remains a grand challenge to map the spatial location of proximal light atoms and to resolve the chemical identity of the first and the second coordination spheres (e.g., C, N, S, etc.) due to their low Z contrast. In addition to STEM, synchrotron-based XAFS provides another powerful tool to probe local information of anchored single atoms. In most cases, metal nanoparticles and atomically dispersed single atoms can be directly differentiated using XAFS. However, the determination of the coordination number and chemical identity of the first and the second coordination spheres via this technique is not straightforward as it often requires a rather delicate match between experimental and theoretical results. Currently, a combination of multiple techniques including STEM, XAFS, and theoretical modeling is required to obtain a relatively reliable determination of local structures. In addition to these widely-used techniques, recent advances in the scanning probe microscopy (e.g., scanning tunneling microscopy

(STM) and noncontact atomic force microscopy (ncAFM)) can be deployed to resolve the local structure of single-atom model catalyst at the single atomic bond level, whereby the adjacent atoms can be mapped out in the real-space.[216–218]

3. It is also crucial to improve molecular-level understanding of the electrocatalytic process over SAECs through the investigation of the adsorption configurations of reactant and intermediates, and their electronic interactions with the active sites. The identification of rate-determining steps will guide the design of efficient electrocatalysts for specific reactions. In many cases, the local structure of the single-atom site undergoes reversible transformations during electrocatalysis. It is highly desired to develop new operando techniques to probe the structural evolution of SAECs due to their chemical interactions with reactant or intermediate species during electrocatalysis. In this regard, *in-situ*/operando characterization techniques and advanced theoretical modelling will be highly valuable. To reduce the complexity of mechanistic studies, the use of model catalysts with well-defined atomic structures can be explored. Recent advances in the computation-aided catalyst design and optimization based on machine learning present new opportunities to accelerate the development of high-performance SAECs with desired local structures toward future industrial applications.

Single-atom electrocatalysts with tunable local environments have shown great promise in diverse renewable energy conversions. The versatile bonding configurations between a single atom and the host offer vast opportunities in constructing the robust and highly efficient SAECs by controlling the first and second coordination spheres and beyond, as well as the host materials. Currently, it is very difficult to categorize different active single atoms and supported materials of SAECs as most of the examples comprise singular structures that give rise to unique performance in specific applications. Moving forward, as techniques for the synthesis and characterization of SAECs become more precise this will enable comparative studies to identify possible trends between promising coordination sites leading to improved function. The joint effort between experimental and theoretical groups will provide new insights into the principles that govern the design and synthesis of well-defined local environments of supported single atoms. The increased research activity will help to address the critical challenges in this field and thus accelerates the development of new-generation SAECs with high activity, selectivity, and stability for a wide range of renewable energy conversions.

Acknowledgements

J.L. acknowledges the support from MOE grants (MOE2017-T2-1-056, R-143-000-A75-114, and R-143-000-B47-114). This work was supported by the National University of Singapore Flagship Green Energy Program (R-279-000-553-646 and R-279-000-553-731).

Conflict of Interest

The authors declare no conflict of interest.

Keywords

electrocatalysis, host engineering, local environments, single atoms

Received: May 6, 2020
Revised: August 6, 2020
Published online:

[1] B. T. Qiao, A. Q. Wang, X. F. Yang, L. F. Allard, Z. Jiang, Y. T. Cui, J. Y. Liu, J. Li, T. Zhang, *Nat. Chem.* **2011**, *3*, 634.
[2] G. Giannakakis, M. F. Stephanopoulos, E. C. H. Sykes, *Acc. Chem. Res.* **2019**, *52*, 237.
[3] A. Q. Wang, J. Li, T. Zhang, *Nat. Rev. Chem.* **2018**, *2*, 65.
[4] H. B. Zhang, G. G. Liu, L. Shi, J. H. Ye, *Adv. Energy Mater.* **2018**, *8*, 1701343.
[5] C. Z. Zhu, S. F. Fu, Q. R. Shi, D. Du, Y. H. Lin, *Angew. Chem., Int. Ed.* **2017**, *56*, 13944.
[6] Y. Cheng, S. Z. Yang, S. P. Jiang, S. Y. Wang, *Small Methods* **2019**, *3*, 1800440.
[7] L. J. Yang, J. L. Shui, L. Du, Y. Y. Shao, J. Liu, L. M. Dai, Z. Hu, *Adv. Mater.* **2019**, *31*, 1804799.
[8] W. J. Zang, Z. K. Kou, S. J. Pennycook, J. Wang, *Adv. Energy Mater.* **2020**, *10*, 1903181.
[9] V. R. Stamenkovic, D. Strmcnik, P. P. Lopes, N. M. Markovic, *Nat. Mater.* **2017**, *16*, 57.
[10] L. Zhang, K. D. Davis, X. L. Sun, *Energy Environ. Sci.* **2019**, *12*, 492.
[11] C. Z. Zhu, Q. R. Shi, S. Feng, D. Du, Y. H. Lin, *ACS Energy Lett.* **2018**, *3*, 1713.
[12] X. Su, X. F. Yang, Y. Q. Huang, B. Liu, T. Zhang, *Acc. Chem. Res.* **2019**, *52*, 656.
[13] Y. Q. Zhang, L. Guo, L. Tao, Y. B. Lu, S. Y. Wang, *Small Methods* **2019**, *3*, 1800406.
[14] B. W. Zhang, Y. X. Wang, S. L. Chou, H. K. Liu, S. X. Dou, *Small Methods* **2019**, *3*, 1800497.
[15] S. Mitchell, E. Vorobyeva, J. Pérez-Ramírez, *Angew. Chem., Int. Ed.* **2018**, *57*, 15316.
[16] H. L. Fei, J. C. Dong, D. L. Chen, T. D. Hu, X. D. Duan, I. Shakir, Y. Huang, X. F. Duan, *Chem. Soc. Rev.* **2019**, *48*, 5207.
[17] Z. B. Liang, C. Qu, D. G. Xia, R. Q. Zou, Q. Xu, *Angew. Chem., Int. Ed.* **2018**, *57*, 9604.
[18] Y. J. Chen, S. F. Ji, C. Chen, Q. Peng, D. S. Wang, Y. D. Li, *Joule* **2018**, *2*, 1242.
[19] X. N. Li, X. F. Yang, J. M. Zhang, Y. Q. Huang, B. Liu, *ACS Catal.* **2019**, *9*, 2521.
[20] L. C. Liu, A. Corma, *Chem. Rev.* **2018**, *118*, 4981.
[21] M. L. Liu, Z. P. Zhao, X. F. Duan, Y. Huang, *Adv. Mater.* **2019**, *31*, 1802234.
[22] A. Kulkarni, S. Siahrostami, A. Patel, J. K. Nørskov, *Chem. Rev.* **2018**, *118*, 2302.
[23] T. Sun, Y. F. Jiang, Q. Wu, L. Y. Du, Z. Q. Zhang, L. J. Yang, X. Z. Wang, Z. Hu, *Catal. Sci. Technol.* **2017**, *7*, 51.
[24] Y. F. Jiang, L. J. Yang, T. Sun, J. Zhao, Z. Y. Lyu, O. Zhuo, X. Z. Wang, Q. Wu, J. Ma, Z. Hu, *ACS Catal.* **2015**, *5*, 6707.
[25] M. L. Pegis, C. F. Wise, D. J. Martin, J. M. Mayer, *Chem. Rev.* **2018**, *118*, 2340.
[26] H. W. Zhang, P. K. Shen, *Chem. Rev.* **2012**, *112*, 2780.
[27] F. Studt, *Catal. Lett.* **2013**, *143*, 58.
[28] L. Z. Zhang, J. M. T. A. Fischer, Y. Jia, X. C. Yan, W. Xu, X. Y. Wang, J. Chen, D. J. Yang, H. W. Liu, L. Z. Zhuang, M. Hankel, D. J. Searles, K. K. Huang, S. H. Feng, C. L. Brown, X. D. Yao, *J. Am. Chem. Soc.* **2018**, *140*, 10757.
[29] W. R. Cheng, X. Zhao, H. Su, F. M. Tang, W. Che, H. Zhang, Q. H. Liu, *Nat. Energy* **2019**, *4*, 115.

[30] Fuel Cell Technical Team Roadmap, U.S. Department of Energy, Fuel Cell Technologies Office, https://www1.eere.energy.gov/vehiclesandfuels/pdfs/program/fctt_roadmap_june2013.pdf (accessed: June 2013).
[31] B. B. Blizanac, P. N. Ross, N. M. Markovic, *Electrochim. Acta* **2007**, *52*, 2264.
[32] B. B. Blizanac, C. A. Lucas, M. E. Gallagher, M. Arenz, P. N. Ross, *J. Phys. Chem. B* **2004**, *108*, 625.
[33] K. L. Svane, M. Reda, T. Vegge, H. A. Hansen, *ChemSusChem* **2019**, *12*, 5133.
[34] W. Jiang, X. L. Zou, H. D. Du, L. Gan, C. J. Xu, F. Y. Kang, W. H. Duan, J. Li, *Chem. Mater.* **2018**, *30*, 2687.
[35] Y. Zheng, Y. Jiao, M. Jaroniec, S. Z. Qiao, *Angew. Chem., Int. Ed.* **2015**, *54*, 52.
[36] W. C. Sheng, H. A. Gasteiger, Y. S. Horn, *J. Electrochem. Soc.* **2010**, *157*, B1529.
[37] B. E. Conway, B. V. Tilak, *Electrochim. Acta* **2002**, *47*, 3571.
[38] J. K. Nørskov, T. Bligaard, A. Logadottir, J. R. Kitchin, J. G. Chen, S. Pandelov, U. Stimming, *J. Electrochem. Soc.* **2005**, *152*, J23.
[39] R. Parsons, *Trans. Faraday Soc.* **1958**, *54*, 1053.
[40] R. Subbaraman, D. Tripkovic, D. Strmcnik, K. C. Chang, M. Uchimura, A. P. Paulikas, V. Stamenkovic, N. M. Markovic, *Science* **2011**, *334*, 1256.
[41] I. L. Yanez, W. D. Z. Wallace, P. S. Pascual, V. Climent, J. M. Feliu, M. T. M. Koper, *Nat. Energy* **2017**, *2*, 17031.
[42] D. Strmcnik, P. P. Lopes, B. Genorio, V. R. Stamenkovic, N. M. Markovic, *Nano Energy* **2016**, *29*, 29.
[43] J. Wang, F. Xu, H. Y. Jin, Y. Q. Chen, Y. Wang, *Adv. Mater.* **2017**, *29*, 1605838.
[44] F. Song, L. C. Bai, A. Moysiadou, S. Lee, C. Hu, L. Liardet, X. L. Hu, *J. Am. Chem. Soc.* **2018**, *140*, 7748.
[45] V. Vij, S. Sultan, A. M. Harzandi, A. Meena, J. N. Tiwari, W. G. Lee, T. Yoon, K. S. Kim, *ACS Catal.* **2017**, *7*, 7196.
[46] P. Tan, B. Chen, H. R. Xu, H. C. Zhang, W. Z. Cai, M. Ni, M. L. Liu, Z. P. Shao, *Energy Environ. Sci.* **2017**, *10*, 2056.
[47] L. L. Zhang, J. Xiao, H. Y. Wang, M. H. Shao, *ACS Catal.* **2017**, *7*, 7855.
[48] P. M. Wood, *Biochem. J.* **1988**, *253*, 287.
[49] N. T. Suen, S. F. Hung, Q. Quan, N. Zhang, Y. J. Xu, H. M. Chen, *Chem. Soc. Rev.* **2017**, *46*, 337.
[50] A. Damjanovic, A. Dey, J. O'M. Bockris, *Electrochim. Acta* **1966**, *11*, 791.
[51] Y. H. Fang, Z. P. Liu, *ACS Catal.* **2014**, *4*, 4364.
[52] Y. Y. Wang, D. F. Yan, S. E. Hankari, Y. Q. Zou, S. Y. Wang, *Adv. Sci.* **2018**, *5*, 1800064.
[53] B. M. Hunter, H. B. Gray, A. M. Müller, *Chem. Rev.* **2016**, *116*, 14120.
[54] C. J. M. van der Ham, M. T. M. Koper, D. G. H. Hetterscheid, *Chem. Soc. Rev.* **2014**, *43*, 5183.
[55] Y. Tanabe, Y. Nishibayashi, *Coord. Chem. Rev.* **2013**, *257*, 2551.
[56] M. A. Shipman, M. D. Symes, *Catal. Today* **2017**, *286*, 57.
[57] C. X. Guo, J. R. Ran, A. Vasileff, S. Z. Qiao, *Energy Environ. Sci.* **2018**, *11*, 45.
[58] X. Y. Cui, C. Tang, Q. Zhang, *Adv. Energy Mater.* **2018**, *8*, 1800369.
[59] E. Skúlason, T. Bligaard, S. Gudmundsóttir, F. Studt, J. Rossmeisl, F. A. Pedersen, T. Vegge, H. Jónsson, J. K. Nørskov, *Phys. Chem. Chem. Phys.* **2012**, *14*, 1235.
[60] Y. Abghoui, A. L. Garden, V. F. Hlynsson, S. Bjorgvinsdóttir, H. Olafsdóttir, E. Skúlason, *Phys. Chem. Chem. Phys.* **2015**, *17*, 4909.
[61] S. D. Minteer, P. Christopher, S. Linic, *ACS Energy Lett.* **2019**, *4*, 163.
[62] B. H. R. Suryanto, H. L. Du, D. B. Wang, J. Chen, A. N. Simonov, D. R. MacFarlane, *Nat. Catal.* **2019**, *2*, 290.
[63] S. Y. Wang, F. Ichihara, H. Pang, H. Chen, J. H. Ye, *Adv. Funct. Mater.* **2018**, *28*, 1803309.
[64] S. Dahl, A. Logadottir, R. C. Egeberg, J. H. Larsen, I. Chorkendorff, E. Törnqvist, J. K. Nørskov, *Phys. Rev. Lett.* **1999**, *83*, 1814.
[65] C. J. H. Jacobsen, S. Dahl, B. S. Clausen, S. Bahn, A. Logadottir, J. K. Nørskov, *J. Am. Chem. Soc.* **2001**, *123*, 8404.
[66] X. Yan, D. L. Liu, H. H. Chen, F. Hou, J. Liang, S. X. Dou, *Small Methods* **2019**, *3*, 1800501.
[67] C. Choi, S. Back, N. Y. Kim, J. Lim, Y. H. Kim, Y. Jung, *ACS Catal.* **2018**, *8*, 7517.
[68] R. J. Lim, M. S. Xie, M. A. Sk, J. M. Lee, A. Fisher, X. Wang, K. H. Lim, *Catal. Today* **2014**, *233*, 169.
[69] J. L. Qiao, Y. Y. Liu, F. Hong, J. J. Zhang, *Chem. Soc. Rev.* **2014**, *43*, 631.
[70] P. Hirunsit, W. Soodsawang, J. Limtrakul, *J. Phys. Chem. C* **2015**, *119*, 8238.
[71] L. M. Wang, W. L. Chen, D. D. Zhang, Y. P. Du, R. Amal, S. Z. Qiao, J. B. Wu, Z. Y. Yin, *Chem. Soc. Rev.* **2019**, *48*, 5310.
[72] Y. H. Wang, J. L. Liu, Y. F. Wang, A. M. Al-Enizi, G. F. Zheng, *Small* **2017**, *13*, 1701809.
[73] Q. Fan, M. L. Zhang, M. W. Jia, S. Z. Liu, J. S. Qiu, Z. Y. Sun, *Mater. Today Energy* **2018**, *10*, 280.
[74] A. J. Martín, G. O. Larrazábal, J. Pérez-Ramírez, *Green Chem.* **2015**, *17*, 5114.
[75] A. A. Peterson, J. K. Nørskov, *J. Phys. Chem. Lett.* **2012**, *3*, 251.
[76] F. C. Vallejo, M. T. M. Koper, *Angew. Chem., Int. Ed.* **2013**, *52*, 7282.
[77] D. Higgins, A. T. Landers, Y. F. Ji, S. Nitopi, C. G. M. Guio, L. Wang, K. Chan, C. Hahn, T. F. Jaramillo, *ACS Energy Lett.* **2018**, *3*, 2947.
[78] W. J. Luo, X. W. Nie, M. J. Janik, A. Asthagiri, *ACS Catal.* **2016**, *6*, 219.
[79] J. K. Li, P. Pršlja, T. Shinagawa, A. J. M. Fernández, F. Krumeich, K. Artyushkova, P. Atanassov, A. Zitolo, Y. C. Zhou, R. G. Muelas, N. López, J. Pérez-Ramírez, F. Jaouen, *ACS Catal.* **2019**, *9*, 10426.
[80] N. Kakati, J. Maiti, S. H. Lee, S. H. Jee, B. Viswanathan, Y. S. Yoon, *Chem. Rev.* **2014**, *114*, 12397.
[81] D. J. Ham, J. S. Lee, *Energies* **2009**, *2*, 873.
[82] K. Sundmacher, T. Schultz, S. Zhou, K. Scott, M. Ginkel, E. D. Gilles, *Chem. Eng. Sci.* **2001**, *56*, 333.
[83] L. Y. Gong, Z. Y. Yang, K. Li, W. Xing, C. P. Liu, J. J. Ge, *J. Energy Chem.* **2018**, *27*, 1618.
[84] T. Whittaker, K. B. Sravan Kumar, C. Peterson, M. N. Pollock, L. C. Grabow, B. D. Chandler, *J. Am. Chem. Soc.* **2018**, *140*, 16469.
[85] C. Bianchin, P. K. Shen, *Chem. Rev.* **2009**, *109*, 4183.
[86] R. Kamai, K. Kamiya, K. Hashimoto, S. Nakanishi, *Angew. Chem., Int. Ed.* **2016**, *55*, 13184.
[87] S. Yamaguchi, K. Kamiya, K. Hashimoto, S. Nakanishi, *Chem. Commun.* **2017**, *53*, 10437.
[88] J. Kim, C. W. Roh, S. K. Sahoo, S. Yang, J. Bae, J. W. Han, H. Lee, *Adv. Energy Mater.* **2018**, *8*, 1701476.
[89] J. J. Gao, J. J. Huo, Y. Liu, W. J. Wu, Y. Wang, M. H. Wu, H. Liu, G. X. Wang, *Small Methods* **2019**, *3*, 1900159.
[90] Z. Q. Zhang, Y. G. Chen, L. Q. Zhou, C. Chen, Z. Han, B. S. Zhang, Q. Wu, L. J. Yang, L. Y. Du, Y. F. Bu, P. Wang, X. Z. Wang, H. Yang, Z. Hu, *Nat. Commun.* **2019**, *10*, 1657.
[91] R. X. Qin, P. X. Liu, G. Fu, N. F. Zheng, *Small Methods* **2018**, *2*, 1700286.
[92] Y. Wang, J. Mao, X. G. Meng, L. Yu, D. H. Deng, X. H. Bao, *Chem. Rev.* **2019**, *119*, 1806.
[93] J. F. Zhang, C. B. Liu, B. Zhang, *Small Methods* **2019**, *3*, 1800481.
[94] C. H. Choi, M. Kim, H. C. Kwon, S. J. Cho, S. Yun, H. T. Kim, K. J. J. Mayrhofer, H. Kim, M. Choi, *Nat. Commun.* **2016**, *7*, 10922.
[95] S. H. Ye, F. Y. Luo, Q. L. Zhang, P. Y. Zhang, T. T. Xu, Q. i Wang, D. S. He, L. C. Guo, Y. Zhang, C. X. He, X. P. Ouyang, M. Gu, J. H. Liu, X. L. Sun, *Energy Environ. Sci.* **2019**, *12*, 1000.
[96] M. Tavakkoli, N. Holmberg, R. Kronberg, H. Jiang, J. Sainio, E. I. Kauppinen, T. Kallio, K. Laasonen, *ACS Catal.* **2017**, *7*, 3121.

[97] S. Q. Chen, N. J. Zhang, C. W. N. Villarrubia, X. Huang, L. Xie, X. Y. Wang, X. D. Kong, H. Xu, G. Wu, J. Zeng, H. L. Wang, *Nano Energy* **2019**, *66*, 104164.
[98] Y. T. Qu, B. X. Chen, Z. J. Li, X. Z. Duan, L. G. Wang, Y. Lin, T. W. Yuan, F. Y. Zhou, Y. D. Hu, Z. K. Yang, C. M. Zhao, J. Wang, C. Zhao, Y. M. Hu, G. Wu, Q. H. Zhang, Q. Xu, B. Y. Liu, P. Gao, R. You, W. X. Huang, L. R. Zheng, L. Gu, Y. E. Wu, Y. D. Li, *J. Am. Chem. Soc.* **2019**, *141*, 4505.
[99] A. Alarawi, V. Ramalingam, J. H. He, *Mater. Today Energy* **2019**, *11*, 1.
[100] H. B. Zhang, P. F. An, W. Zhou, B. Y. Guan, P. Zhang, J. C. Dong, X. W. Lou, *Sci. Adv.* **2018**, *4*, eaao6657.
[101] Q. Qin, T. Heil, M. Antonietti, M. Oschatz, *Small Methods* **2018**, *2*, 1800202.
[102] Z. G. Geng, Y. Liu, X. D. Kong, P. Li, K. Li, Z. Y. Liu, J. J. Du, M. Shu, R. Si, J. Zeng, *Adv. Mater.* **2018**, *30*, 1803498.
[103] J. P. Lai, A. Nsabimana, R. Luque, G. B. Xu, *Joule* **2018**, *2*, 76.
[104] X. P. Yin, H. J. Wang, S. F. Tang, X. L. Lu, M. Shu, R. Si, T. B. Lu, *Angew. Chem., Int. Ed.* **2018**, *57*, 9382.
[105] Y. J. Sa, D. J. Seo, J. Woo, J. T. Lim, J. Y. Cheon, S. Y. Yang, J. M. Lee, D. Kang, T. J. Shin, H. S. Shin, H. Y. Jeong, C. S. Kim, M. G. Kim, T. Y. Kim, S. H. Joo, *J. Am. Chem. Soc.* **2016**, *138*, 15046.
[106] Q. Y. Jia, N. Ramaswamy, H. Hafiz, U. Tylus, K. Strickland, G. Wu, B. Barbiellini, A. Bansil, E. F. Holby, P. Zelenay, S. Mukerjee, *ACS Nano* **2015**, *9*, 12496.
[107] U. I. Kramm, J. Herranz, N. Larouche, T. M. Arruda, M. Lefèvre, F. Jaouen, P. Bogdanoff, S. Fiechter, I. Abs-Wurmbach, S. Mukerjee, J. P. Dodelet, *Phys. Chem. Chem. Phys.* **2012**, *14*, 11673.
[108] E. F. Holby, P. Zelenay, *Nano Energy* **2016**, *29*, 54.
[109] U. I. Kramm, M. Lefèvre, N. Larouche, D. Schmeisser, J. P. Dodelet, *J. Am. Chem. Soc.* **2014**, *136*, 978.
[110] Y. Wang, Y. J. Tang, K. Zhou, *J. Am. Chem. Soc.* **2019**, *141*, 14115.
[111] X. Yang, D. S. Xia, Y. Q. Kang, H. D. Du, F. Y. Kang, L. Gan, J. Li, *Adv. Sci.* **2020**, *7*, 2000176.
[112] H. N. Zhang, J. Li, S. B. Xi, Y. H. Du, X. Hai, J. Y. Wang, H. M. Xu, G. Wu, J. Zhang, J. Lu, J. Z. Wang, *Angew. Chem., Int. Ed.* **2019**, *58*, 14871.
[113] Y. Pan, R. Lin, Y. J. Chen, S. J. Liu, W. Zhu, X. Cao, W. X. Chen, K. L. Wu, W. C. Cheong, Y. Wang, L. R. Zheng, J. Luo, Y. Lin, Y. Q. Liu, C. G. Liu, J. Li, Q. Lu, X. Chen, D. S. Wang, Q. Peng, C. Chen, Y. D. Li, *J. Am. Chem. Soc.* **2018**, *140*, 4218.
[114] H. X. Xu, D. J. Cheng, D. P. Cao, X. C. Zeng, *Nat. Catal.* **2018**, *1*, 339.
[115] Y. Pan, S. J. Liu, K. A. Sun, X. Chen, B. Wang, K. L. Wu, X. Cao, W. C. Cheong, R. A. Shen, A. J. Han, Z. Chen, L. R. Zheng, J. Luo, Y. Lin, Y. Q. Liu, D. S. Wang, Q. Peng, Q. Zhang, C. Chen, Y. D. Li, *Angew. Chem., Int. Ed.* **2018**, *57*, 8614.
[116] X. Wan, X. F. Liu, Y. C. Li, R. H. Yu, L. R. Zheng, W. S. Yan, H. Wang, M. Xu, J. L. Shui, *Nat. Catal.* **2019**, *2*, 259.
[117] C. J. Lei, H. Q. Chen, J. H. Cao, J. Yang, M. Qiu, Y. Xia, C. Yuan, B. Yang, Z. J. Li, X. W. Zhang, L. C. Lei, J. Abbott, Y. Zhong, X. H. Xia, G. Wu, Q. G. He, Y. Hou, *Adv. Energy Mater.* **2018**, *8*, 1801912.
[118] H. L. Fei, J. C. Dong, Y. X. Feng, C. S. Allen, C. Z. Wan, B. Volosskiy, M. F. Li, Z. P. Zhao, Y. L. Wang, H. T. Sun, P. F. An, W. X. Chen, Z. Y. Guo, C. Lee, D. L. Chen, I. Shakir, M. J. Liu, T. D. Hu, Y. D. Li, A. I. Kirkland, X. F. Duan, Y. Huang, *Nat. Catal.* **2018**, *1*, 63.
[119] F. P. Pan, H. G. Zhang, K. X. Liu, D. Cullen, K. More, M. Y. Wang, Z. X. Feng, G. F. Wang, G. Wu, Y. Li, *ACS Catal.* **2018**, *8*, 3116.
[120] Y. Wang, X. Q. Cui, J. X. Zhao, G. R. Jia, L. Gu, Q. H. Zhang, L. K. Meng, Z. Shi, L. R. Zheng, C. Y. Wang, Z. W. Zhang, W. T. Zheng, *ACS Catal.* **2019**, *9*, 336.
[121] H. H. Wu, H. B. Li, X. F. Zhao, Q. F. Liu, J. Wang, J. P. Xiao, S. H. Xie, R. Si, F. Yang, S. Miao, X. G. Guo, G. X. Wang, X. H. Bao, *Energy Environ. Sci.* **2016**, *9*, 3736.
[122] F. Li, G. F. Han, H. J. Noh, S. J. Kim, Y. L. Lu, H. Y. Jeong, Z. P. Fu, J. B. Baek, *Energy Environ. Sci.* **2018**, *11*, 2263.
[123] W. Z. Zheng, J. Yang, H. Q. Chen, Y. Hou, Q. Wang, M. Gu, F. He, Y. Xia, Z. Xia, Z. J. Li, B. Yang, L. C. Lei, C. Yuan, Q. G. He, M. Qiu, X. L. Feng, *Adv. Funct. Mater.* **2020**, *30*, 1907658.
[124] T. Sun, B. B. Tian, J. Lu, C. L. Su, *J. Mater. Chem. A* **2017**, *5*, 18933.
[125] P. N. Duchesne, Z. Y. Li, C. P. Deming, V. Fung, X. J. Zhao, J. Yuan, T. Regier, A. Aldalbahi, Z. Almarhoon, S. W. Chen, D. E. Jiang, N. F. Zheng, P. Zhang, *Nat. Mater.* **2018**, *17*, 1033.
[126] K. Kamiya, R. Kamai, K. Hashimoto, S. Nakanishi, *Nat. Commun.* **2014**, *5*, 5040.
[127] J. Liu, M. G. Jiao, L. L. Lu, H. M. Barkholtz, Y. P. Li, Y. Wang, L. H. Jiang, Z. J. Wu, D. J. Liu, L. Zhuang, C. Ma, J. Zeng, B. S. Zhang, D. S. Su, P. Song, W. Xing, W. L. Xu, Y. Wang, Z. Jiang, G. Q. Sun, *Nat. Commun.* **2017**, *8*, 15938.
[128] J. Kim, C. W. Roh, S. K. Sahoo, S. Yang, J. Bae, J. W. Han, H. Lee, *Adv. Energy Mater.* **2018**, *8*, 1701476.
[129] B. D. Mcnicol, *J. Electroanal. Chem.* **1981**, *118*, 71.
[130] B. Z. Lu, L. Guo, F. Wu, Y. Peng, J. E. Lu, T. J. Smart, N. Wang, Y. Z. Finfrock, D. Morris, P. Zhang, N. Li, P. Gao, Y. Ping, S. W. Chen, *Nat. Commun.* **2019**, *10*, 631.
[131] P. Q. Yin, T. Yao, Y. E. Wu, L. R. Zheng, Y. Lin, W. Liu, H. X. Ju, J. F. Zhu, X. Hong, Z. X. Deng, G. Zhou, S. Q. Wei, Y. D. Li, *Angew. Chem., Int. Ed.* **2016**, *55*, 10800.
[132] Z. L. Wang, X. F. Hao, Z. Jiang, X. P. Sun, D. Xu, J. Wang, H. X. Zhong, F. L. Meng, X. B. Zhang, *J. Am. Chem. Soc.* **2015**, *137*, 15070.
[133] C. M. Zhao, X. Y. Dai, T. Yao, W. X. Chen, X. Q. Wang, J. Wang, J. Yang, S. Q. Wei, Y. E. Wu, Y. D. Li, *J. Am. Chem. Soc.* **2017**, *139*, 8078.
[134] X. L. Zu, X. D. Li, W. Liu, Y. F. Sun, J. Q. Xu, T. Yao, W. S. Yan, S. Gao, C. M. Wang, S. Q. Wei, Y. Xie, *Adv. Mater.* **2019**, *31*, 1808135.
[135] Y. C. Li, X. F. Liu, L. R. Zheng, J. X. Shang, X. Wan, R. M. Hu, X. Guo, S. Hong, J. L. Shui, *J. Mater. Chem. A* **2019**, *7*, 26147.
[136] J. Y. Liu, X. Kong, L. R. Zheng, X. Guo, X. F. Liu, J. L. Shui, *ACS Nano* **2020**, *14*, 1093.
[137] K. Jiang, S. Siahrostami, A. J. Akey, Y. B. Li, Z. Y. Lu, J. Lattimer, Y. F. Hu, C. Stokes, M. Gangishetty, G. X. Chen, Y. W. Zhou, W. Hill, W. B. Cai, D. Bell, K. Chan, J. K. Nørskov, Y. Cui, H. T. Wang, *Chem* **2017**, *3*, 950.
[138] W. X. Chen, J. J. Pei, C. T. He, J. W. Wan, H. L. Ren, Y. Q. Zhu, Y. Wang, J. C. Dong, S. B. Tian, W. C. Cheong, S. Q. Lu, L. R. Zheng, X. S. Zheng, W. S. Yan, Z. B. Zhuang, C. Chen, Q. Peng, D. S. Wang, Y. D. Li, *Angew. Chem., Int. Ed.* **2017**, *56*, 16086.
[139] W. X. Chen, J. J. Pei, C. T. He, J. W. Wan, H. L. Ren, Y. Wang, J. C. Dong, K. L. Wu, W. C. Cheong, J. J. Mao, X. S. Zheng, W. S. Yan, Z. B. Zhuang, C. Chen, Q. Peng, D. S. Wang, Y. D. Li, *Adv. Mater.* **2018**, *30*, 1800396.
[140] Y. Y. Guo, P. F. Yuan, J. N. Zhang, Y. F. Hu, I. S. Amiinu, X. Wang, J. G. Zhou, H. C. Xia, Z. B. Song, Q. Xu, S. C. Mu, *ACS Nano* **2018**, *12*, 1894.
[141] S. Y. Guo, P. F. Yuan, J. N. Zhang, P. B. Jin, H. M. Sun, K. X. Lei, X. C. Pang, Q. Xu, F. Y. Cheng, *Chem. Commun.* **2017**, *53*, 9862.
[142] P. Z. Chen, N. Zhang, T. P. Zhou, Y. Tong, W. S. Yan, W. S. Chu, C. Z. Wu, Y. Xie, *ACS Mater. Lett.* **2019**, *1*, 139.
[143] B. W. Wang, J. X. Zou, X. C. Shen, Y. C. Yang, G. Z. Hu, W. Li, Z. M. Peng, D. Banham, A. G. Dong, D. Y. Zhao, *Nano Energy* **2019**, *63*, 103851.
[144] J. Q. Zhang, Y. F. Zhao, C. Chen, Y. C. Huang, C. L. Dong, C. J. Chen, R. S. Liu, C. Y. Wang, K. Yan, Y. D. Li, *J. Am. Chem. Soc.* **2019**, *141*, 20118.
[145] K. Yuan, D. L. Hecht, L. B. Li, L. Shuai, Y. Z. Li, R. Cao, M. Qiu, X. D. Zhuang, M. K. H. Leung, Y. W. Chen, U. Scherf, *J. Am. Chem. Soc.* **2020**, *142*, 2404.

[146] C. H. Zhang, J. W. Sha, H. L. Fei, M. J. Liu, S. Yazdi, J. B. Zhang, Q. F. Zhong, X. L. Zou, N. Q. Zhao, H. S. Yu, Z. Jiang, E. Ringe, B. I. Yakobson, J. C. Dong, D. L. Chen, J. M. Tour, *ACS Nano* **2017**, *11*, 6930.
[147] Y. H. Han, Y. G. Wang, R. R. Xu, W. X. Chen, L. R. Zheng, A. J. Han, Y. Q. Zhu, J. Zhang, H. B. Zhang, J. Luo, C. Chen, Q. Peng, D. S. Wang, Y. D. Li, *Energy Environ. Sci.* **2018**, *11*, 2348.
[148] X. F. Zhu, X. Tan, K. H. Wu, C. L. Chiang, Y. C. Lin, Y. G. Lin, D. W. Wang, S. Smith, X. Y. Lu, R. Amal, *J. Mater. Chem. A* **2019**, *7*, 14732.
[149] B. X. Zhang, J. L. Zhang, J. B. Shi, D. X. Tan, L. F. Liu, F. Y. Zhang, C. Lu, Z. Z. Su, X. N. Tan, X. Y. Cheng, B. X. Han, L. R. Zheng, J. Zhang, *Nat. Commun.* **2019**, *10*, 2980.
[150] H. C. Kwon, M. Kim, J. P. Grote, S. J. Cho, M. W. Chung, H. Kim, D. H. Won, A. R. Zeradjanin, K. J. J. Mayrhofer, M. Choi, H. Kim, C. H. Choi, *J. Am. Chem. Soc.* **2018**, *140*, 16198.
[151] J. Wang, Z. Q. Huang, W. Liu, C. R. Chang, H. L. Tang, Z. J. Li, W. X. Chen, C. J. Jia, T. Yao, S. Q. Wei, Y. E. Wu, Y. D. Li, *J. Am. Chem. Soc.* **2017**, *139*, 17281.
[152] J. Wang, W. Liu, G. Luo, Z. J. Li, C. Zhao, H. R. Zhang, M. Z. Zhu, Q. Xu, X. Q. Wang, C. M. Zhao, Y. T. Qu, Z. K. Yang, T. Yao, Y. F. Li, Y. Lin, Y. E. Wu, Y. D. Li, *Energy Environ. Sci.* **2018**, *11*, 3375.
[153] G. X. Zhang, Y. Jia, C. Zhang, X. Y. Xiong, K. Sun, R. D. Chen, W. X. Chen, Y. Kuang, L. R. Zheng, H. L. Tang, W. Liu, J. F. Liu, X. M. Sun, W. F. Lin, H. J. Dai, *Energy Environ. Sci.* **2019**, *12*, 1317.
[154] X. F. Zhu, D. T. Zhang, C. J. Chen, Q. R. Zhang, R. S. Liu, Z. H. Xia, L. M. Dai, R. Amal, X. Y. Lu, *Nano Energy* **2020**, *71*, 104597.
[155] Z. Y. Lu, B. Wang, Y. F. Hu, W. Liu, Y. F. Zhao, R. O. Yang, Z. P. Li, J. Luo, B. Chi, Z. Jiang, M. S. Li, S. C. Mu, S. J. Liao, J. J. Zhang, X. L. Sun, *Angew. Chem., Int. Ed.* **2019**, *58*, 2622.
[156] X. P. Han, X. F. Ling, D. S. Yu, D. Y. Xie, L. L. Li, S. J. Peng, C. Zhong, N. Q. Zhao, Y. D. Deng, W. B. Hu, *Adv. Mater.* **2019**, *31*, 1905622.
[157] L. Zhang, R. T. Si, H. S. Liu, N. Chen, Q. Wang, K. Adair, Z. Q. Wang, J. T. Chen, Z. X. Song, J. J. Li, M. N. Banis, R. Y. Li, T. K. Sham, M. Gu, L. M. Liu, G. A. Botton, X. L. Sun, *Nat. Commun.* **2019**, *10*, 4936.
[158] J. Zhang, Q. A. Huang, J. Wang, J. Wang, J. J. Zhang, Y. F. Zhao, *Chin. J. Catal.* **2020**, *41*, 783.
[159] X. J. Zeng, J. L. Shui, X. F. Liu, Q. T. Liu, Y. C. Li, J. X. Shang, L. R. Zheng, R. H. Yu, *Adv. Energy Mater.* **2018**, *8*, 1701345.
[160] D. X. Liu, B. Wang, H. G. Li, S. F. Huang, M. M. Liu, J. Wang, Q. J. Wang, J. J. Zhang, Y. F. Zhao, *Nano Energy* **2019**, *58*, 277.
[161] Q. H. Li, W. X. Chen, H. Xiao, Y. Gong, Z. Li, L. R. Zheng, X. S. Zheng, W. S. Yan, W. C. Cheong, R. G. Shen, N. H. Fu, L. Gu, Z. B. Zhuang, C. Chen, D. S. Wang, Q. Peng, J. Li, Y. D. Li, *Adv. Mater.* **2018**, *30*, 1800588.
[162] H. Sun, M. F. Wang, X. C. Du, Y. Jiao, S. S. Liu, T. Qian, Y. C. Yan, C. Liu, M. Liao, Q. H. Zhang, L. X. Meng, L. Ge, J. Xiong, C. L. Yan, *J. Mater. Chem. A* **2019**, *7*, 20952.
[163] P. Z. Chen, T. P. Zhou, L. L. Xing, K. Xu, Y. Tong, H. Xie, L. D. Zhang, W. S. Yan, W. S. Chu, C. Z. Wu, Y. Xie, *Angew. Chem., Int. Ed.* **2017**, *56*, 610.
[164] Y. J. Chen, S. F. Ji, S. Zhao, W. X. Chen, J. C. Dong, W. C. Cheong, R. G. Shen, X. D. Wen, L. R. Zheng, A. I. Rykov, S. C. Cai, H. L. Tang, Z. B. Zhuang, C. Chen, Q. Peng, D. S. Wang, Y. D. Li, *Nat. Commun.* **2018**, *9*, 5422.
[165] H. J. Shen, E. G. Espino, J. Y. Ma, K. T. Zang, J. Luo, L. Wang, S. S. Gao, X. Mamat, G. Z. Hu, T. Wagberg, S. J. Guo, *Angew. Chem., Int. Ed.* **2017**, *56*, 13800.
[166] Z. L. Jiang, W. M. Sun, H. S. Shang, W. X. Chen, T. T. Sun, H. J. Li, J. C. Dong, J. Zhou, Z. Li, Y. Wang, R. Cao, R. Sarangi, Z. K. Yang, D. S. Wang, J. T. Zhang, Y. D. Li, *Energy Environ. Sci.* **2019**, *12*, 3508.
[167] K. Yuan, S. Sfaelou, M. Qiu, D. L. Hecht, X. D. Zhuang, Y. W. Chen, C. Yuan, X. L. Feng, U. Scherf, *ACS Energy Lett.* **2018**, *3*, 252.
[168] W. Zhang, K. K. Mao, X. C. Zeng, *ACS Sustainable Chem. Eng.* **2019**, *7*, 18711.
[169] K. L. Wu, X. Chen, S. J. Liu, Y. Pan, W. C. Cheong, W. Zhu, X. Cao, R. A. Shen, W. X. Chen, J. Luo, W. S. Yan, L. R. Zheng, Z. Chen, D. S. Wang, Q. Peng, C. Chen, Y. D. Li, *Nano Res.* **2018**, *11*, 6260.
[170] L. L. Cao, Q. Q. Luo, W. Liu, Y. Lin, X. K. Liu, Y. J. Cao, W. Zhang, Y. E. Wu, J. L. Yang, T. Yao, S. Q. Wei, *Nat. Catal.* **2019**, *2*, 134.
[171] H. B. Yang, S. F. Hung, S. Liu, K. D. Yuan, S. Miao, L. P. Zhang, X. Huang, H. Y. Wang, W. Z. Cai, R. Chen, J. J. Gao, X. F. Yang, W. Chen, Y. Q. Huang, H. M. Chen, C. M. Li, T. Zhang, B. Liu, *Nat. Energy* **2018**, *3*, 140.
[172] C. C. Yan, H. B. Li, Y. F. Ye, H. H. Wu, F. Cai, R. Si, J. P. Xiao, S. Miao, S. H. Xie, F. Yang, Y. S. Li, G. X. Wang, X. H. Bao, *Energy Environ. Sci.* **2018**, *11*, 1204.
[173] X. G. Fu, N. Li, B. H. Ren, G. P. Jiang, Y. R. Liu, F. M. Hassan, D. Su, J. B. Zhu, L. Yang, Z. Y. Bai, Z. P. Cano, A. P. Yu, Z. W. Chen, *Adv. Energy Mater.* **2019**, *9*, 1803737.
[174] R. Jiang, L. Li, T. Sheng, G. F. Hu, Y. G. Chen, L. Y. Wang, *J. Am. Chem. Soc.* **2018**, *140*, 11594.
[175] X. Rong, H. J. Wang, X. L. Lu, R. Si, T. B. Lu, *Angew. Chem., Int. Ed.* **2020**, *59*, 1961.
[176] X. Q. Wei, X. Luo, H. J. Wang, W. L. Gu, W. W. Cai, Y. H. Lin, C. Z. Zhu, *Appl. Catal., B* **2020**, *263*, 118347.
[177] Y. D. Mun, S. Lee, K. Kim, S. Kim, S. Lee, J. W. Han, J. Lee, *J. Am. Chem. Soc.* **2019**, *141*, 6254.
[178] T. Sun, G. Q. Zhang, D. Xu, X. Lian, H. X. Li, W. Chen, C. L. Su, *Mater. Today Energy* **2019**, *12*, 215.
[179] X. Lyu, G. Li, X. K. Chen, B. W. Shi, J. Z. Liu, L. Z. Zhuang, Y. Jia, *Small Methods* **2019**, *3*, 1800450.
[180] C. Y. Wang, W. X. Chen, K. L. Xia, N. H. Xie, H. M. Wang, Y. Y. Zhang, *Small* **2019**, *15*, 1804966.
[181] K. W. Mou, Z. P. Chen, X. X. Zhang, M. Y. Jiao, X. P. Zhang, X. Ge, W. Zhang, L. C. Liu, *Small* **2019**, *15*, 1903668.
[182] L. C. Bai, C. S. Hsu, D. T. L. Alexander, H. M. Chen, X. L. Hu, *J. Am. Chem. Soc.* **2019**, *141*, 14190.
[183] Y. Pan, C. Zhang, Z. Liu, C. Chen, Y. D. Li, *Matter* **2020**, *2*, 78.
[184] S. Yang, Y. J. Tak, J. Kim, A. Soon, H. Lee, *ACS Catal.* **2017**, *7*, 1301.
[185] S. K. Sahoo, Y. J. Ye, S. Lee, J. Park, H. Lee, J. Lee, J. W. Han, *ACS Energy Lett.* **2019**, *4*, 126.
[186] S. Yang, J. Kim, Y. J. Tak, A. Soon, H. Lee, *Angew. Chem., Int. Ed.* **2016**, *55*, 2058.
[187] X. Liu, Y. Jiao, Y. Zheng, K. Davey, S. Z. Qiao, *J. Mater. Chem. A* **2019**, *7*, 3648.
[188] L. L. Chen, Y. L. Zhang, L. L. Dong, W. X. Yang, X. J. Liu, L. Long, C. Y. Liu, S. J. Dong, J. B. Jia, *J. Mater. Chem. A* **2020**, *8*, 4369.
[189] Z. H. Pu, I. S. Amiinu, R. L. Cheng, P. Y. Wang, C. T. Zhang, S. C. Mu, W. Y. Zhao, F. M. Su, G. X. Zhang, S. J. Liao, S. H. Sun, *Nano-Micro Lett.* **2020**, *12*, 21.
[190] Y. Y. Liu, J. J. Wu, K. P. Hackenberg, J. Zhang, Y. M. Wang, Y. C. Yang, K. Keyshar, J. Gu, T. Ogitsu, R. Vajtai, J. Lou, P. M. Ajayan, B. C. Wood, B. I. Yakobson, *Nat. Energy* **2017**, *2*, 17127.
[191] Y. N. Guo, T. Park, J. W. Yi, J. Henzie, J. Kim, Z. L. Wang, B. Jiang, Y. Bando, Y. Sugahara, J. Tang, Y. Yamauchi, *Adv. Mater.* **2019**, *31*, 1807134.
[192] J. Deng, H. B. Li, J. P. Xiao, Y. C. Tu, D. H. Deng, H. X. Yang, H. F. Tian, J. Q. Li, P. J. Ren, X. H. Bao, *Energy Environ. Sci.* **2015**, *8*, 1594.
[193] N. N. Xuan, J. H. Chen, J. J. Shi, Y. W. Yue, P. Y. Zhuang, K. Ba, Y. Y. Sun, J. F. Shen, Y. Y. Liu, B. H. Ge, Z. Z. Sun, *Chem. Mater.* **2019**, *31*, 429.
[194] H. J. Liu, Q. He, H. L. Jiang, Y. X. Lin, Y. K. Zhang, M. Habib, S. M. Chen, L. Song, *ACS Nano* **2017**, *11*, 11574.
[195] J. Deng, H. B. Li, S. H. Wang, D. Ding, M. S. Chen, C. Liu, Z. Q. Tian, K. S. Novoselov, C. Ma, D. H. Deng, X. H. Bao, *Nat. Commun.* **2017**, *8*, 14430.

[196] W. Y. Zhou, S. S. Li, X. Y. Xiao, S. H. Chen, J. H. Liu, X. J. Huang, *Chem. Commun.* **2018**, *54*, 9329.
[197] H. B. Zhang, L. Yu, T. Chen, W. Zhou, X. W. Lou, *Adv. Funct. Mater.* **2018**, *28*, 1807086.
[198] R. C. Luo, M. Luo, Z. Q. Wang, P. Liu, S. X. Song, X. D. Wang, M. W. Chen, *Nanoscale* **2019**, *11*, 7123.
[199] Y. P. Zang, S. W. Niu, Y. S. Wu, X. S. Zheng, J. Y. Cai, J. Ye, Y. F. Xie, Y. Liu, J. B. Zhou, J. F. Zhu, X. J. Liu, G. M. Wang, Y. T. Qian, *Nat. Commun.* **2019**, *10*, 1217.
[200] W. Xiao, P. T. Liu, J. Y. Zhang, W. D. Song, Y. P. Feng, D. Q. Gao, J. Ding, *Adv. Energy Mater.* **2017**, *7*, 1602086.
[201] T. Sun, J. Wang, X. Chi, Y. X. Lin, Z. X. Chen, X. Ling, C. T. Qiu, Y. S. Xu, L. Song, W. Chen, C. L. Su, *ACS Catal.* **2018**, *8*, 7585.
[202] K. A. Sun, L. Y. Zeng, S. H. Liu, L. Zhao, H. Y. Zhu, J. C. Zhao, Z. Liu, D. W. Cao, Y. C. Hou, Y. Q. Liu, Y. Pan, C. G. Liu, *Nano Energy* **2019**, *58*, 862.
[203] Z. Y. Luo, Y. X. Ouyang, H. Zhang, M. L. Xiao, J. J. Ge, Z. Jiang, J. L. Wang, D. M. Tang, X. Z. Cao, C. P. Liu, W. Xing, *Nat. Commun.* **2018**, *9*, 2120.
[204] K. Qi, X. Q. Cui, L. Gu, S. S. Yu, X. F. Fan, M. C. Luo, S. Xu, N. B. Li, L. R. Zheng, Q. H. Zhang, J. Y. Ma, G. Yue, F. Lv, K. Wang, H. H. Huang, W. Zhang, S. J. Guo, T. W. Zheng, P. Liu, *Nat. Commun.* **2019**, *10*, 5231.
[205] J. M. Zhang, X. P. Xu, L. Yang, D. J. Cheng, D. P. Cao, *Small* **2019**, *3*, 1900653.
[206] I. H. Kwak, I. S. Kwon, H. G. Abbas, G. Jung, Y. Lee, T. T. Debela, S. J. Yoo, J. G. Kim, J. Park, H. S. Kang, *Nanoscale* **2018**, *10*, 14726.
[207] Z. G. Chen, W. B. Gong, Z. B. Liu, S. Cong, Z. H. Zheng, Z. Wang, W. Zhang, J. Y. Ma, H. S. Yu, G. H. Li, W. B. Lu, W. C. Ren, *Nano Energy* **2019**, *60*, 394.
[208] N. Zhang, T. P. Zhou, M. L. Chen, H. Feng, R. L. Yuan, C. A. Zhang, W. S. Yan, Y. C. Tian, X. J. Wu, W. S. Chu, C. Z. Wu, Y. Xie, *Energy Environ. Sci.* **2020**, *13*, 111.
[209] X. Hai, X. X. Zhao, N. Guo, C. H. Yao, C. Chen, W. Liu, Y. H. Du, H. Yan, J. Li, Z. X. Chen, X. Li, Z. J. Li, H. M. Xu, P. Lyu, J. Zhang, M. Lin, C. L. Su, S. J. Pennycook, C. Zhang, S. B. Xi, J. Lu, *ACS Catal.* **2020**, *10*, 5862.
[210] Q. Z. Xiong, Y. Wang, P. F. Liu, L. R. Zheng, G. Z. Wang, H. G. Yang, P. K. Wong, H. M. Zhang, H. J. Zhao, *Adv. Mater.* **2018**, *30*, 1801450.
[211] L. Zhao, Y. Zhang, L. B. Huang, X. Z. Liu, Q. H. Zhang, C. He, Z. Y. Wu, L. J. Zhang, J. P. Wu, W. L. Yang, L. Gu, J. S. Hu, L. J. Wan, *Nat. Commun.* **2019**, *10*, 1278.
[212] Y. Cheng, S. Y. Zhao, B. Johannessen, J. P. Veder, M. Saunders, M. R. Rowles, M. Cheng, C. Liu, M. F. Chisholm, R. D. Marco, H. M. Cheng, S. Z. Yang, S. P. Jiang, *Adv. Mater.* **2018**, *30*, 1706287.
[213] E. Antolini, *Appl. Catal., B* **2009**, *88*, 1.
[214] Y. H. He, S. W. Liu, C. Priest, Q. R. Shi, G. Wu, *Chem. Soc. Rev.* **2020**, *49*, 3484.
[215] Y. Y. Liu, Y. M. Wang, B. I. Yakobson, B. C. Wood, *Phys. Rev. Lett.* **2014**, *113*, 028304.
[216] L. Gross, F. Mohn, N. Moll, P. Liljeroth, G. Meyer, *Science* **2009**, *325*, 1110.
[217] L. Gross, F. Mohn, N. Moll, G. Meyer, R. Ebel, W. M. Abdel-Mageed, M. Jaspars, *Nat. Chem.* **2010**, *2*, 821.
[218] J. Su, M. Telychko, P. Hu, G. Macam, P. Mutombo, H. J. Zhang, Y. Bao, F. Cheng, Z. Q. Huang, Z. Z. Qiu, S. J. R. Tan, H. Lin, P. Jelinek, F. C. Chuang, J. S. Wu, J. Lu, *Sci. Adv.* **2019**, *5*, eaav7717.

Tao Sun is a research fellow in Jiong Lu's group at the Department of Chemistry, Centre for Advanced 2D Materials, National University of Singapore (NUS). He received his Ph.D. degree in Physical Chemistry in 2016 from Nanjing University. His research interest focuses on the design and synthesis of nanomaterials for electrochemical energy conversions, especially for the single-atom electrocatalysts.

Sharon Mitchell is a lecturer in the group of Advanced Catalysis Engineering at ETH Zurich. Prior to this position she completed her Ph.D. at the University of Cambridge, and undertook postdocs at the Institute of Chemical Research of Catalonia and ETH Zurich. Her research focuses on the precision design of catalytic materials, including those based on single atoms, toward sustainable technologies. To this end, nanostructuring approaches are coupled with the advanced characterization of structure–property relationships over appropriate length and time scales.

Javier Pérez-Ramírez holds the chair of Catalysis Engineering at ETH Zurich. His research pursues the design of heterogeneous catalysts and reactor concepts tackling current and future energy, resource, and environmental challenges of society. He directs a National Competence Center of Research in Catalysis in Switzerland and has a visiting appointment at the National University of Singapore within the Flagship Green Energy Program.

Jiong Lu holds assistant professorship at the Department of Chemistry, Centre for Advanced 2D Materials, National University of Singapore (NUS). He received his Bachelor's degree from Fudan University, Ph.D. degree from NUS, and then did postdoctoral research in Department of Physics, University of California, Berkeley. His current research interests include atomic-scale imaging and characterization of 2D materials and their devices, and single-atom and single-cluster catalysis for environmental and energy related applications.